Electronic excitations in Topological Insulators

studied by Electron Energy Loss Spectroscopy

by

Ganesh Subramanian

A Thesis Presented in Partial Fulfillment
of the Requirements for the Degree
Master of Science

Approved October 2013 by the
Graduate Supervisory Committee:

John. C. H. Spence, Chair
Allen Nan Jiang
Tingyong Chen
Candace Chan

ARIZONA STATE UNIVERSITY

December 2013

ABSTRACT

Topological insulators with conducting surface states yet insulating bulk states have generated a lot of interest amongst the physics community due to their varied characteristics and possible applications. Doped topological insulators have presented newer physical states of matter where topological order co-exists with other physical properties (like magnetic order). The electronic states of these materials are very intriguing and pose the problems and the possible solutions to understanding their unique behaviors.

In this work, we use Electron Energy Loss Spectroscopy (EELS) – an analytical TEM tool to study both core-level and valence-level excitations in Bi_2Se_3 and $Cu(doped)Bi_2Se_3$ topological insulators. We use this technique to retrieve information on the valence, bonding nature, co-ordination and lattice site occupancy of the undoped and the doped systems. Using the reference materials Cu(I)Se and Cu(II)Se we try to compare and understand the nature of doping that copper assumes in the lattice. And lastly we utilize the state of the art monochromated Nion UltraSTEM 100 to study electronic/vibrational excitations at a record energy resolution from sub-nm regions in the sample.

ACKNOWLEDGMENTS

It has been a great 2.5 years at Dr. John Spence's group. My first thanks are due to Dr. Amish Shah. Within the 1 month that we had together, he got me into the work and group ethics and stood through probably the most stupid portions of my alter ego. Most importantly, he ramped me into TEM and definitely deserves a sincere and friendly acknowledgement.

Dr. Nan Jiang has been a very close part of our research right from the start. John holds him in very high regard and it has always been fun interacting with Dr. Nan Jiang regarding core-loss EELS and FEFF. Saturdays could be interesting as well … and the few times I had met him on a Saturday, I got to know his kid ☺ We probably have a longer journey to ride together and so I will reserve my complete appreciation of all his support for a little later!

Shibom Basu – the nature man :D … partner at crime [except the whole world would know that he is upto something even before he makes up his mind … lightning fast is he ;)]. The best compliment he ever received for his TA – 'He has a great dressing sense'. Im disappointed every time he comes back alone from California … If I were to ever trust myself to an investment banker, it would have to be him :D

Nadia – easily the most neat and well-dressed physicist I have come across! I think Shibom and I together give her a hard fight to keep the average presentation sense for our group as low as possible :D Music is always an interesting subject to discuss … need to find the right occasions to do more with her … And ohh, she is a big fan of Bikram yoga – a yoga mat and tons of sweat is all one needs to get her best wishes ☺.

ii

Dingjie and Dan are my sole compatriots. With all the action happening in the neighboring room, they give me a feel of relief to know im not the only person sitting alone in a window-less room!

Yuin … I have to be careful talking to him because sometimes when I joke I don't know if he takes it as an offense ☺ On a totally unrelated note, I will get demoralized if I sit next to him for 5 minutes … I can never study as much as him.

Chufeng Li – and his gang of friends :D … Chufeng reminds me exactly of what I would have caricatured as a Chinese monk. I hope I did good enough to give him a decent opinion of the group and work ethic. A lot to share with him and about him … a bigger acknowledgement is in store for him, just a little later!

Toshi is the 'in' man … If one had to assess popularity votes, he would be the most sought after person in the TEM area in ASU (leaving out administration). A lot to learn from him and his experience … im really looking forward to the onward journey ☺

And finally John - easily the most fun person I have met so far. Lots of energy and a very practical lifestyle is almost characteristic of him. Asking for opinion is the best part of interaction with John … when he is in mood he is very witty and it can make your day. Lots and lots to learn … Lots to observe from close and far. I owe the biggest thanks to him and hope to be inspired for many more years to come.

TABLE OF CONTENTS

LIST OF ABBREVIATIONS

EELS – Electron Energy Loss Spectroscopy

MC – Monochromator

FWHM – Full Width at Half Maximum

ZLP – Zero Loss Peak

IR – Infra Red

STEM – Scanning Transmission Electron Microscopy

CFEG – Cold-Field Emission Gun

ABF – Annular Bright Field

MAADF – Medium-angle Annular Dark Field

HAADF – High-angle Annular Dark Field

CCD – Charge-coupled device

ELS – Energy Loss Spectroscopy

DOS – Density of States

LL – Landau Levels

QHE – Quantum Hall Effect

IQHE – Integer Quantum Hall Effect

QSH – Quantum Spin Hall

SQHE – Spin Quantum Hall Effect

TI – Topological Insulator

ARPES – Angle-Resolved Photoemission Spectroscopy

2DEG – Two Dimensional Electron Gas

VB – Valence Band

CB – Conduction Band

HR-TEM – High Resolution - Transmission Electron Microscopy

EDS – Energy Dispersive X-ray Spectroscopy

FIB – Focused Ion Beam

BF – Bright Field

ZA – Zone-Axis

NEFS – Near-edge fine structure

XANES – X-ray absorption near-edge structure

LDOS – Local-density of states

RSMS – Real-space multiple scattering

ELNES – Energy Loss near-edge structure

XAS – X-ray absorption spectroscopy

TDOS – Total-density of states

AC-STEM – Aberration correction Scanning Transmission Electron Microscopy

ROI – Region of Interest

LIST OF FIGURES

CHAPTER 1

INTRODUCTION

1.1   Electron Energy Loss Spectroscopy

When fast moving electrons interact with a material, the Coulombic (electrostatic) forces due to the atoms present in the material scatter the incident electrons. Such scattering causes the incident electrons to change the direction of their momenta and, many a time, also lose energy. If a spectrometer is attached to the side facing the transmitted electron beam, that can record and resolve the energy of the electron beam hitting it, we have the potential of studying various different natures of interactions of the probe (electron) with electrostatic forces within the material (atom and atomic-electrons). This process is described as Electron Energy Loss Spectroscopy (EELS) [1]. It is so named because it studies the energy lost by the incident electrons in interacting with matter as it comes out as the transmitted beam.

Incident electrons as they travel through a sample can go through various experiences. A majority of the electrons do no interact with any of the atoms and thus pass through unscathed. In the language of the EEL spectroscopists, we term this as the 'Zero-loss' regime. Of those electrons that interact with the material, the two major contributors to the scattering of the incident electrons are (a) the nucleus and (b) atomic-electrons. The nucleus is a dense bundle of charge and hence the deflection off a nucleus is generally very large. In other words, these are typically responsible for very high scattering angles of the incident beam. This is christened as 'Elastic Scattering'. This kind of scattering leads to the formation of a diffraction pattern (periodic arrangement of the nuclei is reflected by the interference of the electron waves that are scattered off the

nuclei). In addition to this, the lattice vibrations (collective mechanical motion of the atom centers - called as phonons) also scatter the incident electrons. But such interactions result in very small energy losses (one-tenth of an eV or lesser). These kind of electron-phonon interactions have been difficult to study using EELS for many reasons. Recent developments in instrumentation, though, may have broken through this barrier. We will talk more about this in the next section.

Albeit being a dense bundle of charge, the nucleus is small in comparison to the vast regions of space present around it. (Typical nuclear radius is 10^{-5} A° while typical atomic radius is 1 A° and interatomic distances in a crystal are generally about 2-3A°). Surrounding the nucleus are the atomic-electrons and the incident electrons can interact with these electrons too. These sorts of interactions typically involve a considerable energy exchange and hence are termed 'Inelastic Scattering'. All atomic-electrons do not behave similar while interacting with the incident beam. In a typical electron-electron interaction, the atomic-electron absorbs energy from the incident beam to excite and make a transition to the unoccupied electronic states above the Fermi level. To compensate for the 'hole' now created in such an excitation, a de-excitation process soon follows in which an electron from a higher electronic state than that of the initial state of the excited electron, drops down. Excess energy (if any) will thus be liberated as x-rays or the kinetic energy of another atomic electron (Auger emission). Inner-shell electrons have ground-state energies that are a few hundred eV lower than the Fermi level. Such interactions have scattering angles of the order of a few 10s of mrad and are typically single-electron transitions. The energy loss recorded on the spectrometer is few 100s of eVs and this regime is termed as the 'Core-Loss' regime.

2

Outer-shell electrons also undergo similar single-electron transitions as long as they have enough energy (obtained from the incident beam) to excite across the energy gap (for semiconductors and insulators) and other higher electronic states (for metals). But they are more typically known for their collective excitations as 'plasmons'. The fundamental idea behind such collective excitations is the possibility to share the excess energy amongst the participating outer-shell atomic-electrons. Both these processes are found to occur at energy losses at around 5-30 eV. This is termed as the 'Low Loss' regime.

Each of the above mentioned regimes posses different valuable information regarding the crystal structure, bonding, coordination, density of electronic states, valence etc. Discussing each of these would in itself be a huge task and thus, as and when we require, appropriate theoretical basis and interpretation will be provided in those sections.

The schematic of an incident electron beam scattering in a material is shown in fig (1.1.i). A representative EELS spectrum is with the different regimes labeled is shown in fig (1.1.ii).
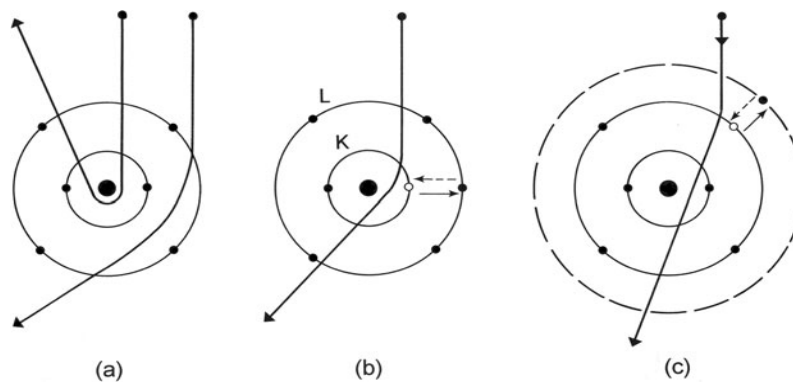

Fig (1.1.i) Schematic of electron scattering off an atom. (a) is the representative diagram for elastic scattering off a nucleus. (b) is a diagram showing core (inner-shell) atomic-electron excitation and de-excitation (depicted using broken arrows). (c) is a similar representation for the interaction with outer-shell electrons.

3
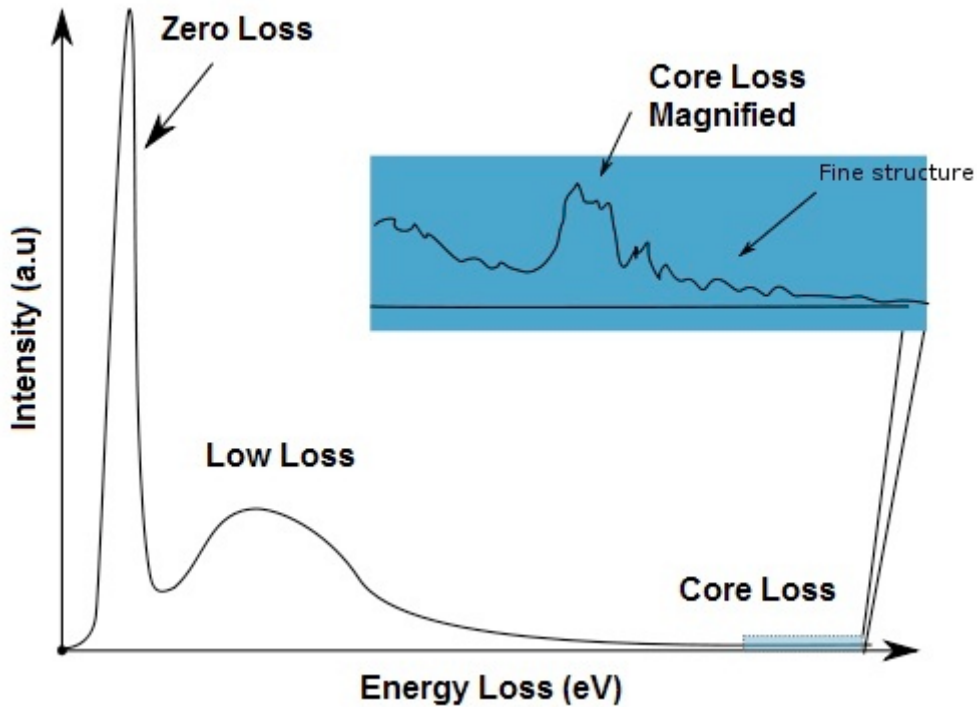
Fig (1.1.ii) Representative image of an EEL spectrum. The different regions are marked appropriately and the core-loss region magnified in the inset. Since the EEL spectrum is cumulative the background of the spectrum increases with energy loss.

1.2 Nion UltraSTEM^{TM}100MC at ASU

The latest addition to the list of TEMs at ASU is the Nion UltraSTEM^{TM}100MC [2]. The Nion is a stand-alone STEM instrument and the latest versions of their designs have C_3 and C_5 aberration correctors. In this version (the latest of them all) however, the addition to the instrument is a mono-chromator (MC). The schematic of the instrument is presented in fig (1.2.i). The presence of the MC reduces the FWHM of the ZLP by more than a factor of 10 and as a routine now, the instrument offers 40-50 meV energy resolution. This is a big step ahead because the instrument is unique in being able to offer 50 meV energy resolution coupled with sub-nm spatial resolution. In a sense, this clubs together the positives of IR/Raman spectroscopy (ability to probe phonon modes) with STEM (ability to offer <3A° spatial resolution).

4

The relevance of this instrument with our work will become obvious in the latter sections.
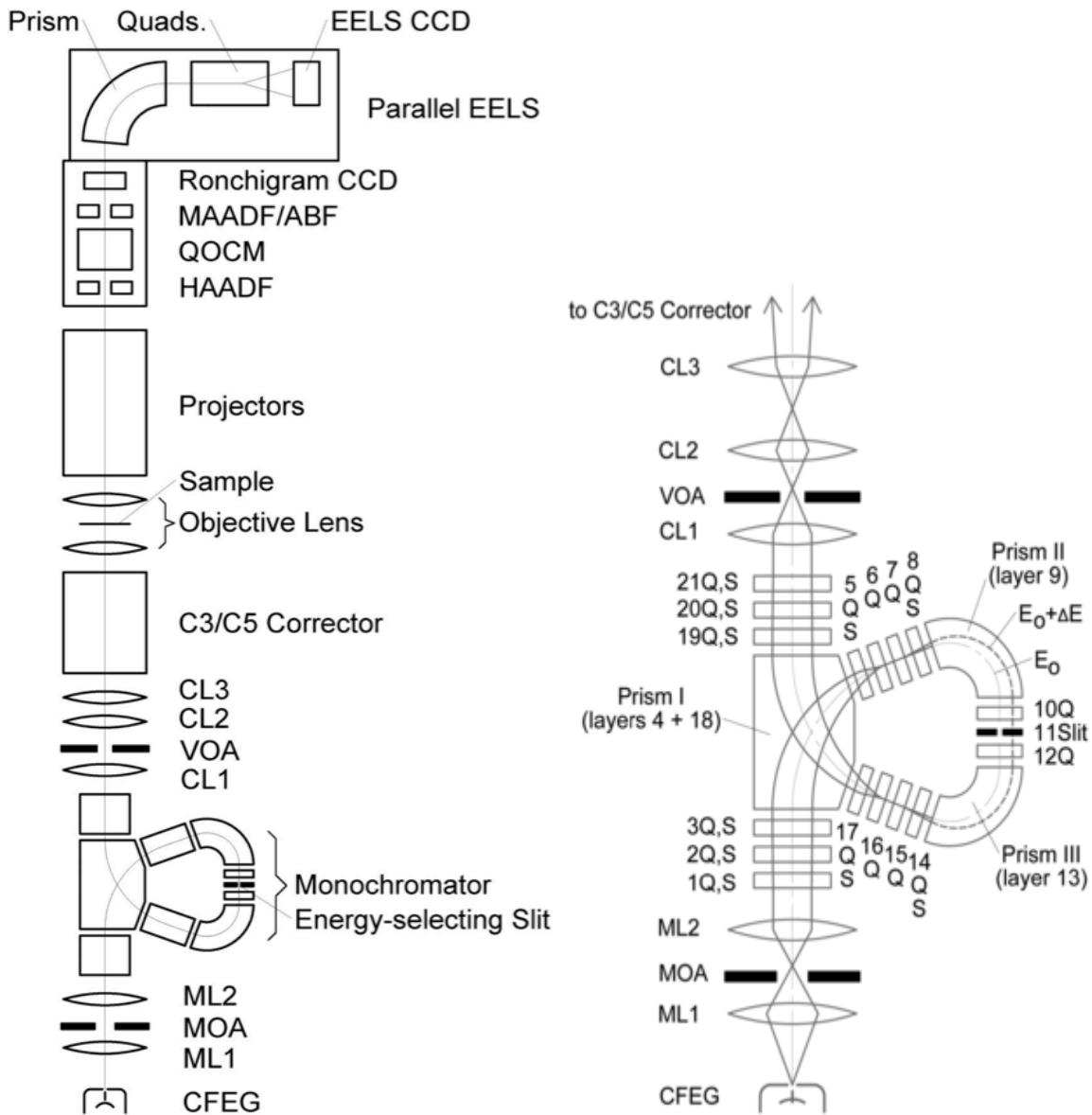
Fig (1.2.i) LEFT: Schematic of the Nion UltraSTEM^{TC}100MC installed at ASU. The gun (CFEG) is located at the bottom. The electron beam passes the MC aperture into the slit where the energy selection is made. After narrowing down the beam, it passes through a set of condenser lenses and then the aberration correctors. At this point the beam interacts with the sample and passing through the projector lenses it is received by various detectors. As a typical STEM instrument, it supports ABF, MAADF and HAADF. There is a CCD placed to view the ronchigram and past all that is the ELS detector.
RIGHT: Schematic of the cross-section of the MC showing all lenses and the slit.

1.3   Topological Insulators

Topological insulators are a new class of materials identified by the scientific community as recently as in 2008 [3] where the bulk of the material is insulating while the surface is conducting. Interestingly, one can observe dissipation-less transport of electric current on any of the 6 surfaces of the material subject to certain conditions. This has opened a flurry of interesting properties/applications [4] which include:

- Dissipation-less transport

- Spintronics applications

- Fault-tolerant Quantum Computing

- Experimental observation of Majorana Physics

- Topological Superconductors

But the identification of these materials has not been sudden and unexpected. It is possible to track a serial evolution of the idea of this sort of a property. It all started with the classical 'Hall Effect'. On application of an electric field perpendicular to a magnetic field in a current carrying material, one can observe a voltage drop across the material in the 3rd direction read as the Hall voltage or the Hall resistance. This can be observed from fig (1.3.i). The characteristics of Hall Effect are thus –

- External Electric Field present
- External Magnetic Field present
- Continuous Energy Levels observed
- Typically 3D materials.
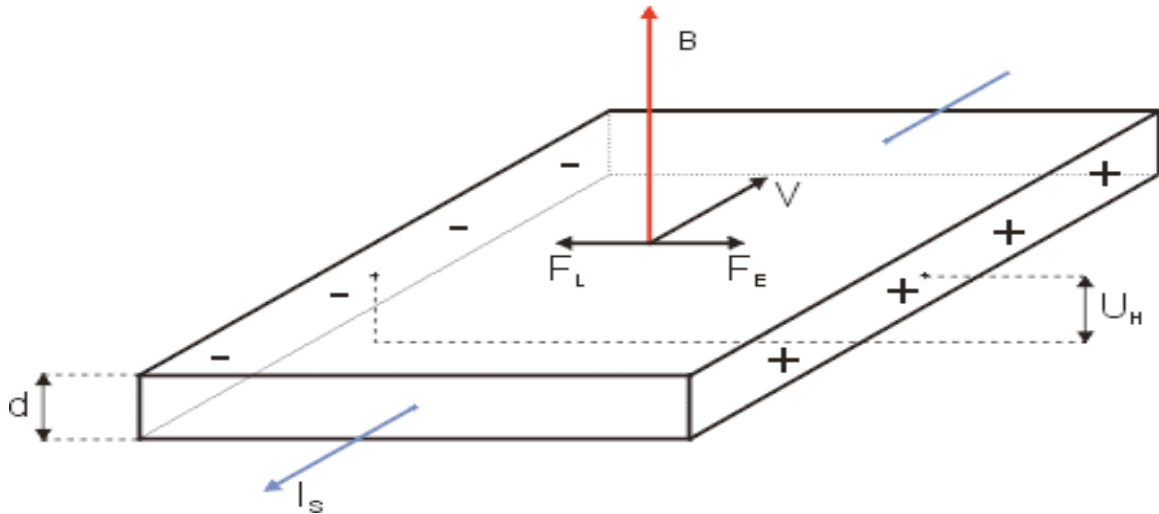
Fig (1.3.i) Schematic of the Hall Effect. The magnetic field (B) is out of plane and the direction of the electric field is the denoted by the direction of the current (I_S). F_L and F_E show the directions of the Lorentz forces. U_H is the difference between the potentials along the width of the sample which is defined as the Hall voltage.

With the growth of instruments and measuring capabilities, scientists were interested in observing Hall Effect for 2D samples (when the thickness was brought down to a few nm). When this study was done at low temperature (<10K) and high magnetic fields (3-10T), the resistance did not vary linearly anymore. More importantly, the electron transport was mapped to identify existence of 'edge-states' that were the only conducting path for the electrons. This is demonstrated in fig (1.3.ii). The 2D-DOS (supposed to be independent of energy) in the presence of a magnetic field clumps into Landau Levels (LL) separated by the cyclotron energy. Thus the DOS (and hence resistance) was no more monotonic. This was termed the Quantum Hall Effect [5] and its characteristics are -

- External Electric field present

- External Magnetic field present

- Energy levels are quantized (not continuous)

- Very thin 2D materials
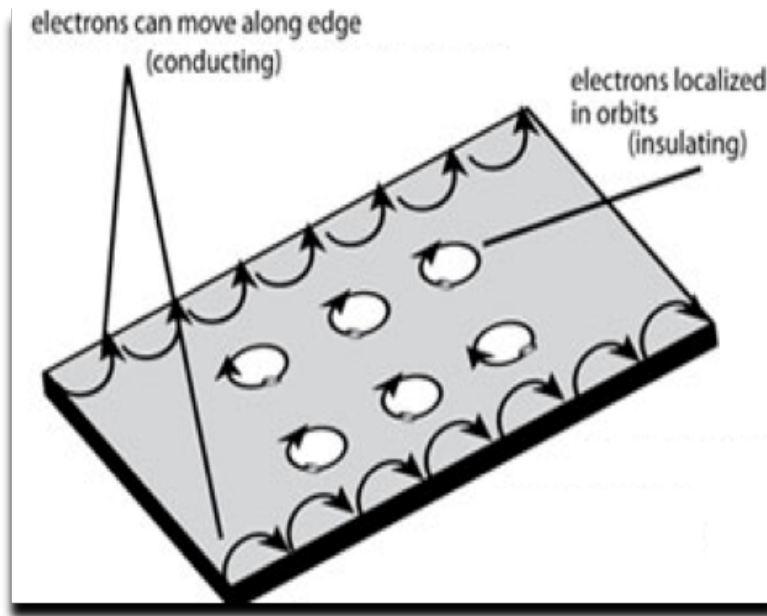
Fig (1.3.ii) Electron Motion in the Quantum Hall Effect. The schematic shows the presence of edge states (propogation of the electrons only on the edge of the 2D system). We can notice that those electrons whose cyclotron orbits are well within the boundaries do not contribute to any current. They become localized and insulating states.

The Quantum Spin Hall (QSH) [6] state is a state of matter proposed to exist in special, 2D semiconductors with spin-orbit coupling. The QSH is a cousin of the integer QH state, but, unlike the latter, it does not require the application of a large magnetic field. It is very important here to note that the QSH state does not break any discrete symmetries (such as time-reversal or parity) unlike the other previously mentioned effects.

The first proposal for the existence of a quantum spin Hall state was developed by Kane and Mele [7] who adapted an earlier model for graphene by Haldane et.al (proposed in 1988) which exhibits an IQHE. The Kane and Mele model is, two copies of the Haldane model one over the other, such that the spin up electron exhibits a chiral-IQHE while the spin down electron exhibits an anti-chiral IQHE. Very recently (in 2006) was a
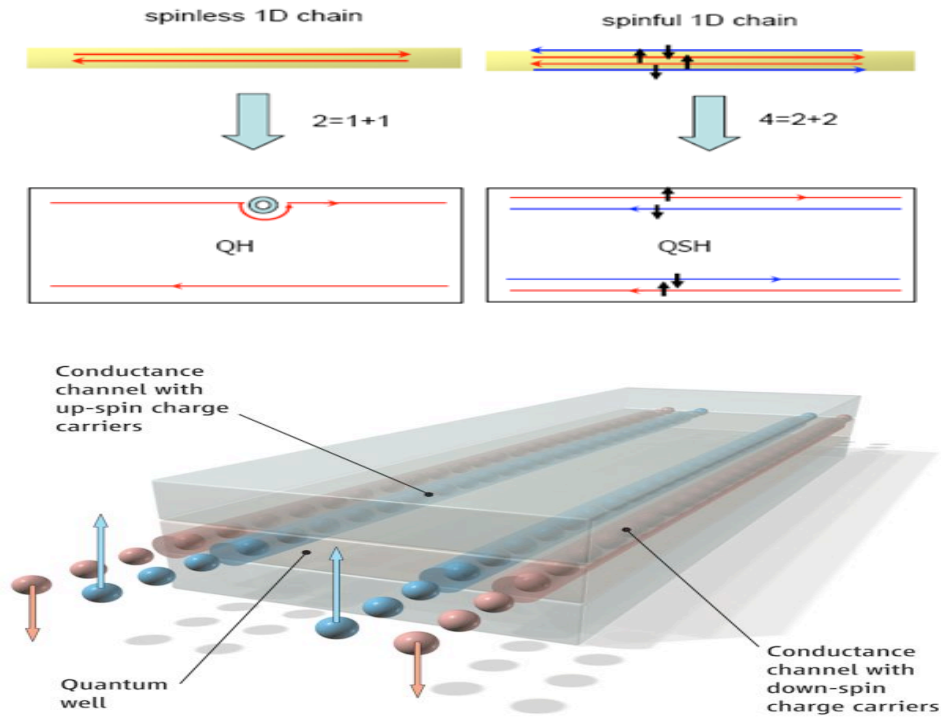
Fig(1.3.iii) Schematic for electron transport in QSHE. TOP: Displaying the conceptual difference between a QHE and QSHE in terms of the effect of spins and the order of the forward moving and reverse moving wave-vectors of the spins. Note also that for every channel there are 2 electrons of opposite spins moving in opposite directions together. BOTTOM: Schematic 3D representation of transport through a QSH state of the sandwiched HgTe layers.

proposal of theoretical work [8] subsequently experimentally realized [9] in the (HgTe) Mercury(II)Telluride semiconductors. Overall the Kane-Mele model has a charge-Hall conductance of exactly 'zero' but a spin-Hall conductance of $2(e/4\pi)$. A schematic visualization of the QSHE is presented in fig (1.3.iii). In this kind of a system -

- External Electric field present

- External Magnetic field absent!

- Energy levels are quantised (not continous)

- Sandwiched 2D interfaces (few monolayers)

The concept of topologically protected states as proposed by Kane and Mele [6,10] triggered a lot of interest and opened up the possibility of new materials which could exhibit similar properties, as mentioned in the above cases, although not necessarily through the same mechanism. A Topological Insulator (TI) is a material that behaves as an insulator in its interior or bulk while permitting the movement of charges (metallic/semi-metallic) on its surface. In the bulk of a topological insulator, the electronic band structure resembles an ordinary band insulator with the Fermi level in the band gap. On the surface of a topological insulator though, there are special states that allow surface metallic conduction. Carriers in these surface states have their spin locked at a right angle to their momentum (spin-momentum locking or topological order). At a given energy the only other available electronic states have opposite spin, so the "U"-turn scattering is strongly suppressed and conduction on the surface is highly metallic. These states are characterized by an index (known as Z2 topological invariants) and are an example of topologically ordered states.

Topologically protected edge states (like SQHE) were predicted to occur in quantum wells (very thin layers) of mercury telluride sandwiched between cadmium telluride and was observed shortly thereafter. But the surprise came when they were also predicted to occur in three dimensional bulk solids [11] of binary compounds involving 'Bismuth'. The first experimentally realized 3D topological insulator state was discovered in bismuth antimony [3]. The Z2 topological invariants cannot be measured using traditional transport methods since it requires the separation of surface conduction from that of the bulk. Hence only a surface characterization technique, like ARPES, could resolve the spin-sensitive momentum and thereby help differentiate between the bulk and edge states in

the system. We can refer to fig (1.3.iv) for the same. Eventually, topologically protected surface states were also observed in antimony, bismuth selenide, bismuth telluride and antimony telluride using ARPES.
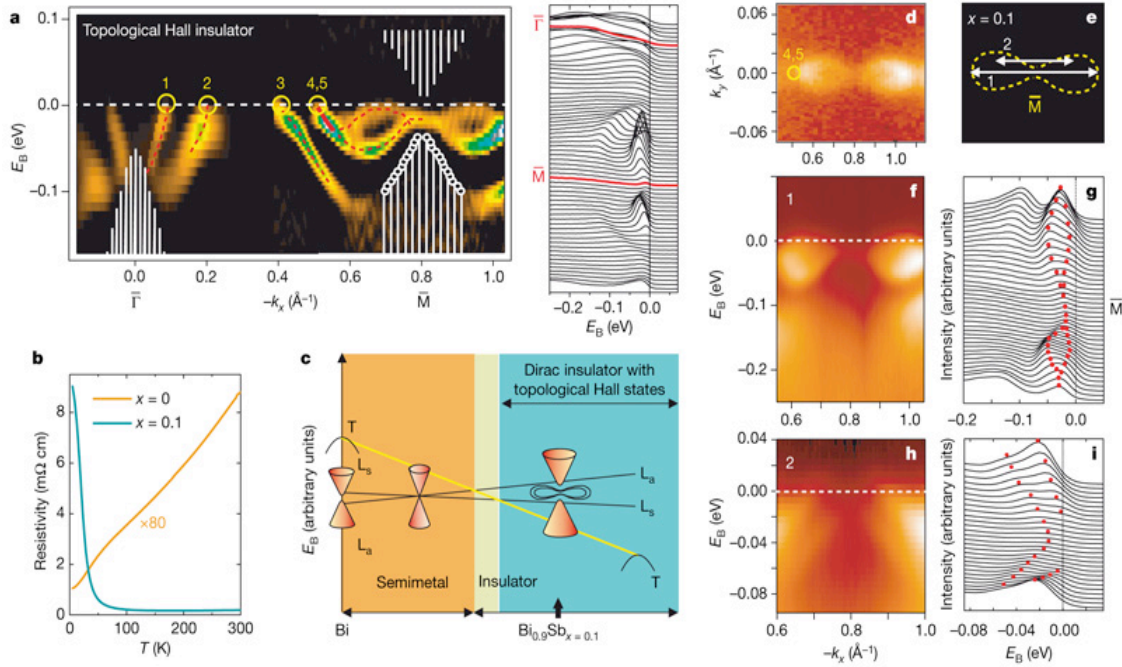
Fig (1.3.iv) ARPES results on Bi-Sb. A: the number of edge states (corresponds to number of cross-overs and it has to be odd) resolved. B: resistivity measurements done on Bi and $Bi_{0.9}$-$Sb_{0.1}$ devices. C: Schematic of the edge state conduction in the Bi-Sb system. (D-I): The Evolution of the Dirac cones in the band structure as the Energy of the probe is altered to resolve the edge state and line-plot along the dotted line.

The surface states of a 3D Topological insulator are thus a new type of 2DEG (two dimensional electron gas) where electron's spin is locked to its linear momentum. In a sense it is an extension of the edge-states in a 2D QHE. All the six surfaces possess these states. The point to note though, is that, the mechanisms for these two processes are

11

not really related. Moreover, although they posses a Dirac-cone like band structure, the topological surface states differ from Graphene due to the locking of spin and momentum. Thus as a summary, in characteristics of TIs are:

- External Electric field present

- External Magnetic field absent!

- Energy levels are quantized (not continuous)

- Bulk 3D materials!

1.4   Bismuth Selenide

Bismuth Selenide (Bi_2Se_3) is a TI with a bulk band gap of around 0.32 eV. It belongs to the Tetradymite family with an R-3m space group. The lattice parameters are: a = b = 4.138 A° and c = 28.636 A°. We can refer to Fig (1.4.i) for the unit-cell structure along specific orientations.

Although it is very recent that Bi_2Se_3 has been identified as a TI [12], both Bi_2Se_3 and Bi_2Te_3 have for long been studied as thermoelectric materials. But Bi_2Se_3 is a comfortable candidate to work with because of its relatively higher band gap. Further it has a single surface state implying simpler detection and analysis of the same. Inherently it is known to possess two kinds of defects [13] – Bi_{Se} (anti-site defects) and V_{Se} (Selenium vacancies). That apart, researchers have doped Bi_2Se_3 with various elements as Ca, Mn, Fe, Cu, Au, Sm etc [14–16], each with a particular property or effect in mind – to reduce the vacancy induced un-intentional n-doping; to observe the coupled simultaneous behavior of magnetic and surface effects; to observe variation in thermoelectric coefficients with interaction/non-interaction of surface states etc. Specifically Cu-Bi_2Se_3 [17,18] displays

12

superconductivity for T < 10K and this is simultaneous to the presence of the surface states − a topological superconductor! Understanding this is touted to be a big stepping-stone in realizing quantum computers. This is where our interest in the material arose.

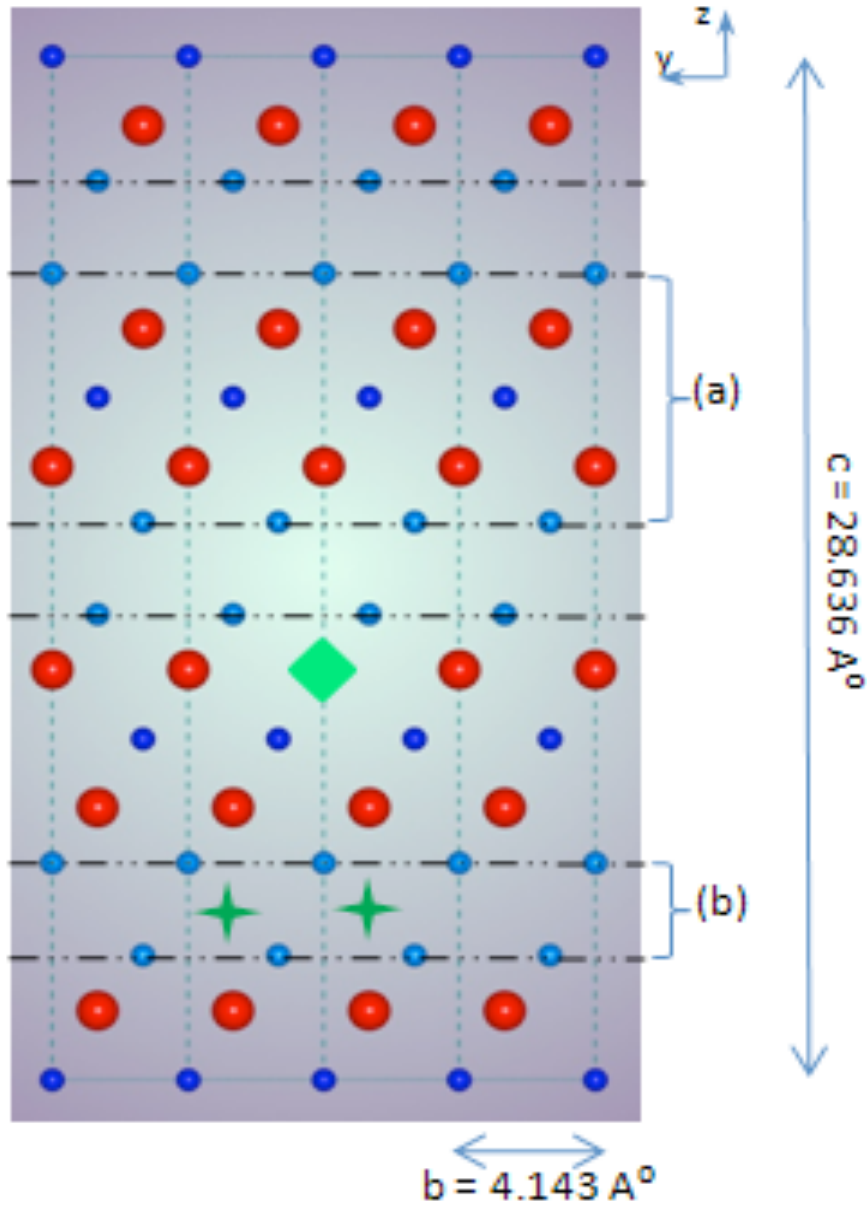Fig (1.4.i) Bi_2Se_3 crystal structure. Unit cell viewed along (100). The red atoms correspond to Bi. The dark and light blue atoms correspond to Se (at two non-equivalent sites). The green square and the green stars are the possible sites for dopant atoms to substitute Bi and intercalate in the van der Waals, respectively, gap represented by (b). (a) corresponds to a single set of quintuple layers [Se_1-Bi-Se_2-Bi-Se_1].

Very recently a few articles have been published in journals that talk of the issue of studying Bi_2Se_3 using TEM and related analytical methods. In the article by Huang et al. [19], they perform a HAADF-STEM based structural analysis on bulk-grown Bi_2Se_3 to identify Bi anti-site defects. This was immediately followed by Liou et al. [20,21] where they perform angle-resolved TEM-EELS and STEM-EELS experiments on Bi_2Se_3 to identify the various peaks in the low-loss regime. They clarify an issue of the 6.3eV plasmon peak of being bulk in origin (as opposed to prior experiments predicting a surface plasmon nature). They also perform Molecular Orbital calculations to present a theoretical basis for their prior claim in the following article. Finally there was a very recent article by Da et al. [22] where they do HR-TEM studies on $Cu-Bi_2Se_3$ and using phase reconstruction mechanisms they detect the interstitial Copper atoms located in the Bi_2Se_3 lattice.

Thus, our aim for the experiments boiled down to two big issues – (i) to identify the position and local environment of the dopant atom (Cu) in the host lattice (Bi_2Se_3) to help understand the interaction between magnetic order and topological order and (ii) understand the effect of local crystal environment on the electronic properties of Bi_2Se_3 close to the Fermi level. We immediately realized that both these objectives are obtainable using the EELS technique: the core-loss EELS [23] would provide information regarding the local environment around the dopant Cu atom – the position, co-ordination, and valence; the low-loss EELS would provide a list of all the electronic transitions occurring close the VB-CB region. Thus, the quest to study electronic transitions in Bi_2Se_3 and $Cu- Bi_2Se_3$ using EELS began…

CHAPTER 2

EXPERIMENTS

2.1   Samples, instruments and softwares

The Bi_2Se_3 and Cu- Bi_2Se_3 samples were grown using the Bridgeman technique and obtained from Dr. Yulin Chen from Stanford University (now at Oxford, UK). These are bulk crystals and the dopant concentration was 2-3%. The reference samples of 99.95% Cu(I)Se were obtained from Sigma Aldrich and 99.5% Cu(II)Se were obtained from Alfa Aesar. Au-mesh grids of #400 mesh and #1000 mesh were obtained from Ted Pella and used to deposit the TEM samples of these materials.

The TEM samples were prepared using Leica Ultracut R ultramicrotome. HR-TEM imaging and TEM-EDS and EELS experiments were performed on the Jeol 2010F. Most of the HAADF-STEM imaging and STEM-EELS of the Cu(II)Se samples were done using the Jeol ARM 200F. Some of the HAADF-STEM imaging and STEM-EELS of Cu(II)Se and all of them for Bi_2Se_3 were performed on the Nion UltraSTEM^{TM}100MC.

HAADF-STEM image simulations for Cu(II)Se and Bi_2Se_3 were performed using the STEMSLICE program from Dr. E. Kirkland. The ELNES and DOS calculations for the core-loss EELS for Cu(II)Se, Cu(I)Se, Bi_2Se_3 and Cu- Bi_2Se_3 were performed using the FEFF8.4 code.

All EELS data analysis was performed using the Digital Micrograph 2010. Crystal structure and diffraction simulations were done using the CrystalMaker software package.

2.2 TEM Sample preparations

Bi_2Se_3 is anisotropic (as can be observed from the unit cell parameters) and is weakly bonded in the c-axis (van der Waals force between each quintuple layer). Therefore, similar to Graphene, it can be easily exfoliated along the a-b plane. This makes it tough to prepare TEM samples because polishing these samples will crush/break them very easily. FIB and other such milling processes induce a lot of damage (and defects) to the sample thus altering their structural character. Moreover the samples are not grown on a substrate (these are bulk grown). So it is all the more vulnerable to losing integrity. Thus we had to identify a method of sample preparation that can utilize this as it is and yet make samples that are thin enough to be studied by HRTEM and STEM. This is when we stumbled upon 'Ultramicrotomy'.

As we can see in fig (2.2.i), ultramicrotomy is the process of using a diamond/glass knife to manually/automatically cut thin sections of a given material. This follows two steps – (i) To embed the material in a resin and then let it age for a couple of days to harden as a matrix. (ii) To position this matrix on the microtome stage and then set the knife to cut through this matrix (cutting sections of the resin+material). Prior knowledge of the orientation of the material can help in suitably embedding it in the resin so that when the sections are cut, they are very close to the required directions. Further, the sample holder is generally fitted with a vernier gauge that permits to change the angle of the sample with respect to the knife in 2 directions in the plane parallel to the knife. Once this is fixed and calibrated, the first sections of the material is cut at larger thicknesses (200nm-500nm) to get a feel of the friction offered on the knife as it passes through the region with the material. At this point if there is no harm happening to the

sections, then it is safe to turn the vernier lower so as to obtain thinner sections. The instrument we use, Leica Ultracut R, can produce sections of the order of $20 - 30$ nm consistently. Below this is not consistent and not predictable. It is very important to choose the right resin to as a matrix to host the desired material. The criterion to be looked at is the hardness of sample must be comparable to the hardness of the resin.
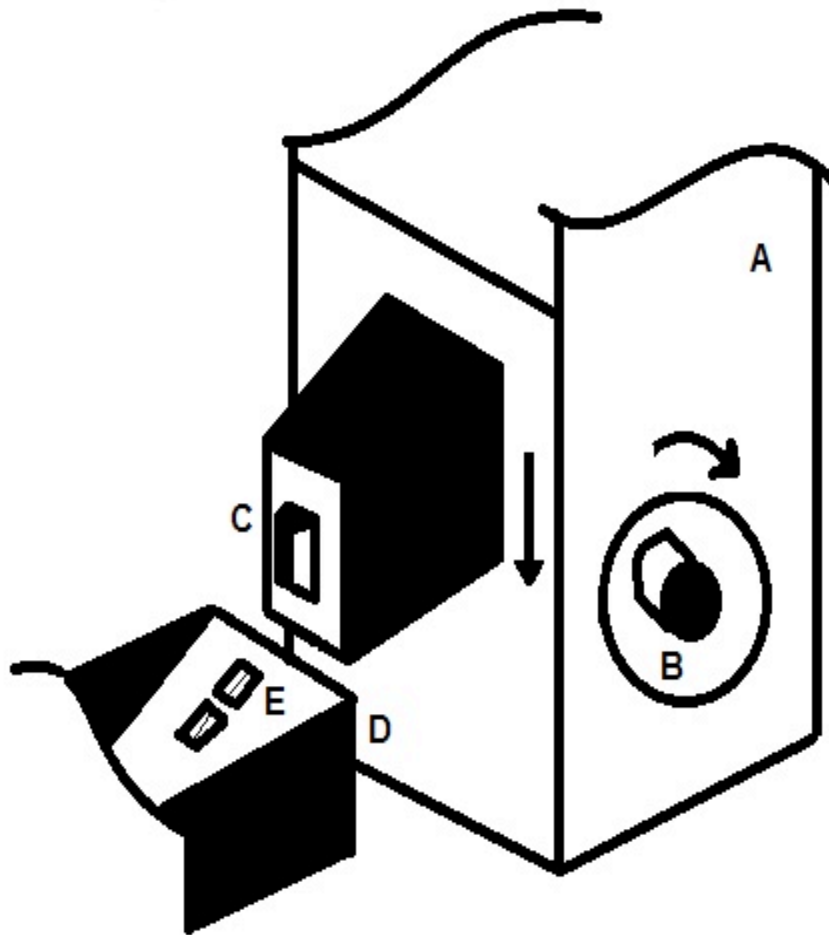
Fig (2.2.i) Schematic of the microtome knife and the stage. A: Sample stage. B: Manual knob which on rotation (clockwise) brings the sample-stage down and then raises it back up. C: Sample (resin+material) set on the sample stage. D: Diamond/Glass knife. E: Sections coming off the knife edge and collection into the hollow filled with water. Eventually the TEM grid is dipped from a side, beneath the sections, to collect them on the grid. Use a small filter paper to remove excess water and the sample is ready for TEM analysis.

Ultramicrotomy is typically used for polymers, biological materials and other soft-materials that cannot withstand traditional polishing and/or milling techniques used to prepare TEM samples. A very big advantage of the method is that it uses substantially less raw material to prepare the final sample in comparison to polishing methods.

For our work, all our samples were prepared using this method. The resin we used is Epon and we prepared both plan-view and cross-sections of Bi_2Se_3, Cu-Bi_2Se_3, $Cu(I)Se$ and $Cu(II)Se$.

2.3   2010F and Core-Loss EELS

2.3.1   Preliminary TEM

Once the samples are ready, we take them to the Jeol 2010F instrument. Typically this sample is spread out over large regions. And so to start with the high-mag mode might not be a good idea. It is important to identify the sample regions and then increment in magnification. A very important step here is to get used to the difference between strips of resin sections and strips of sample sections. Simple logic will guide us to realize that the scattering of the sample region will be stronger and so in BF imaging, the material of interest (Bi_2Se_3 or Cu-Se) will appear much darker than the resin.

Fig (2.3.1.i) shows relatively low-mag images of the sample on the mesh-grids. It is important to note here that although the sample might have been identified, there might still be resin beneath the sample. Depending on how thick the resin layer beneath is, it might/might not affect spectroscopic information obtained from the sample region. So it is important to be patient in finding a good region with minimal/no resin (carbon) layers beneath the material.
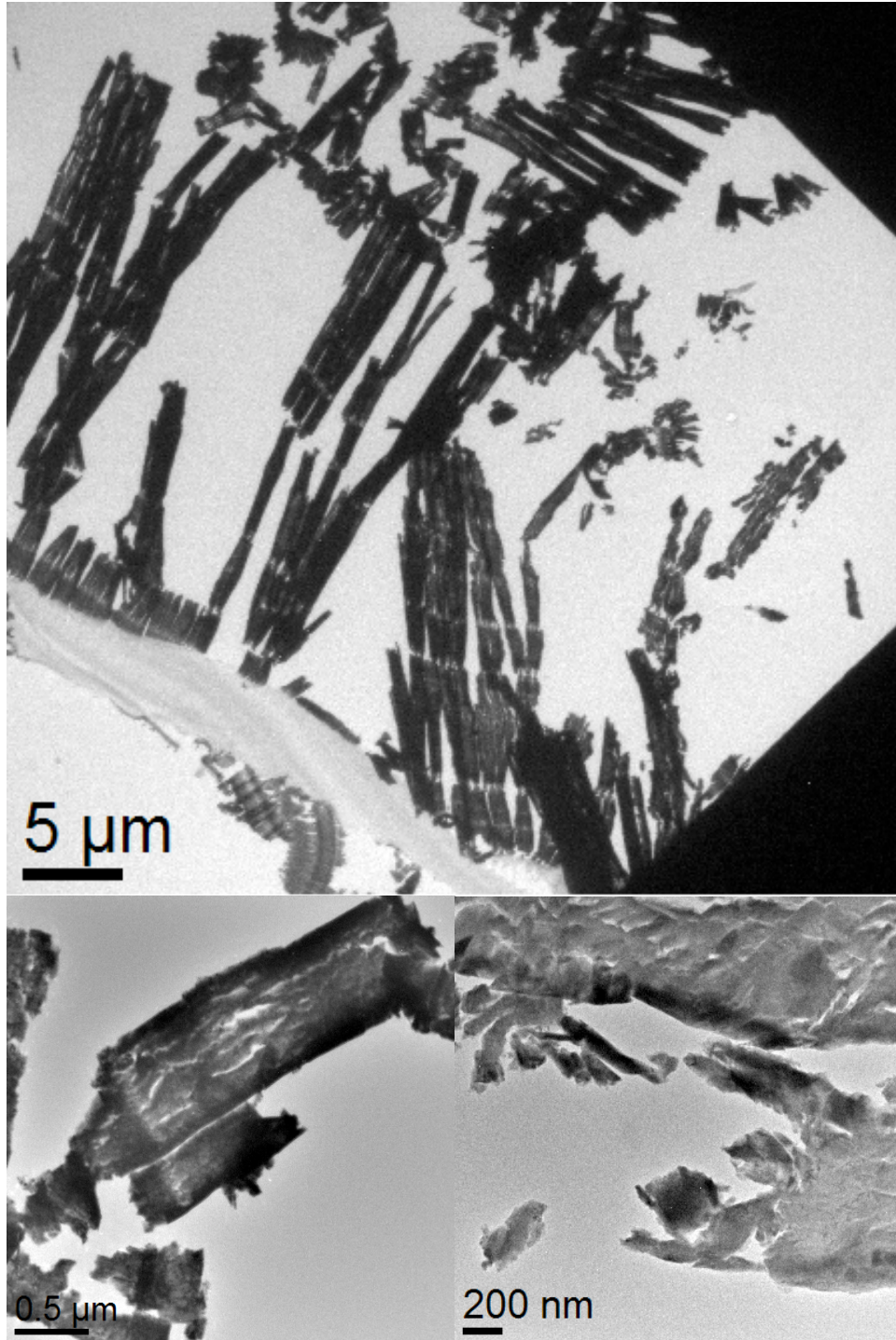
Fig (2.3.1.i) TOP: Low-mag TEM image of the Bi_2Se_3 sample region. The solid black region to the top and bottom right of the image is the Au-mesh grid. The stronger scattering darker regions are the Bi_2Se_3 sample sections and the relatively thinner strip running perpendicular at the bottom left of the image is a section of the resin. BOTTOM LEFT and BOTTOM RIGHT are higher magnification images focusing into a sample region. Note that the sample sections can get folded over each other.

19
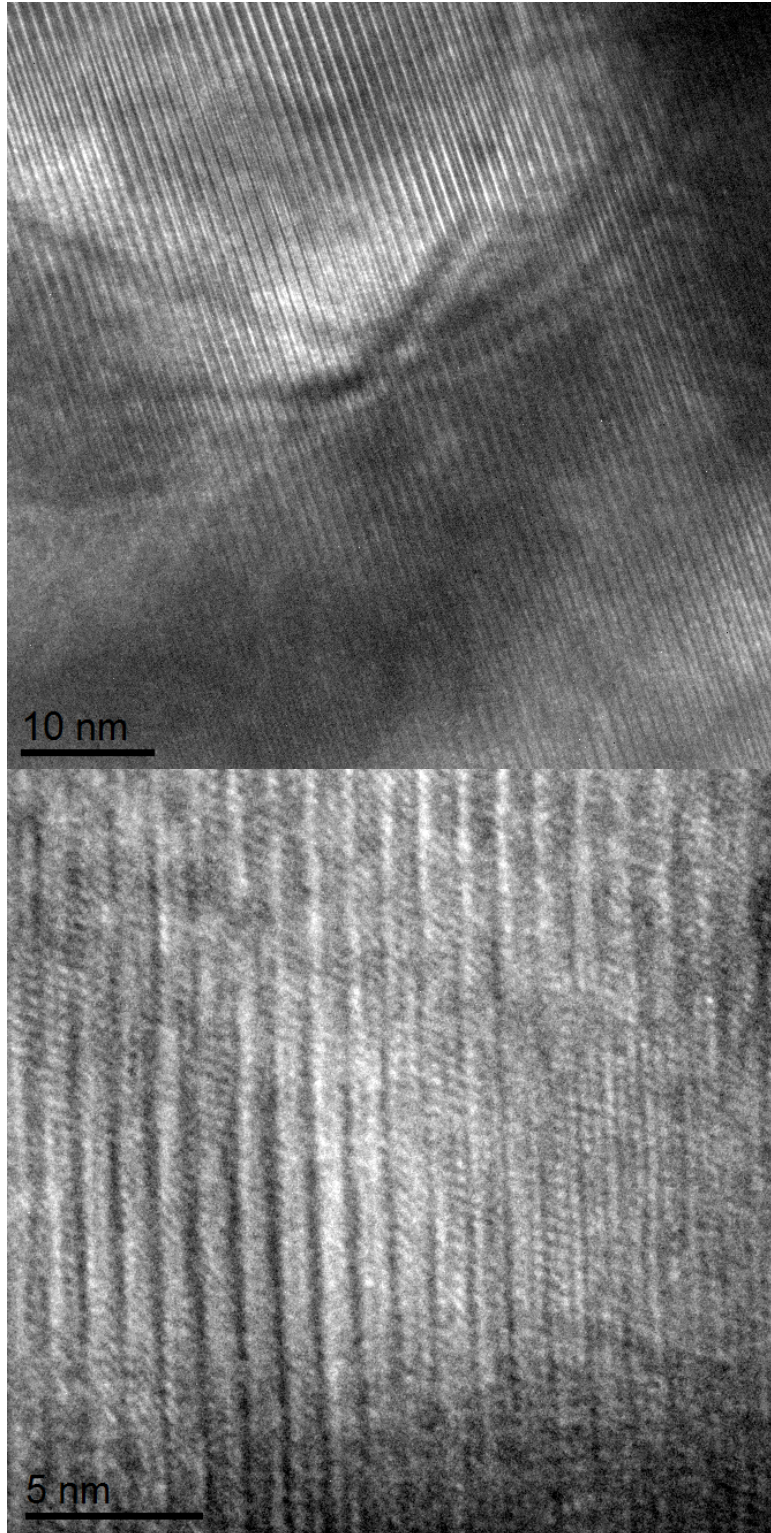
Fig (2.3.1.ii) HRTEM images at high-mag of cross-sectional Bi_2Se_3. Sample prepared using TOP: 25nm sections and BOTTOM: 50nm sections. Notice the intereference patterns reflecting the quintuple layer sequence in both images. Neither of the images were taken at a ZA orientation.

Fig (2.3.1.iii) EDS spectrum of Cu-Bi$_2$Se$_3$. Sample N3D region-1 showing clear indication of Cu-Kα peak and thus presence of Cu. It also highlights Se-Lα, Bi-Lα, Au-Lα, Bi-Lβ, Au-Lβ peaks amongst others. Note that some of the peaks are very close and hence overlap. Hence its imperative to find peaks without overlaps for quantitative analysis (if any).

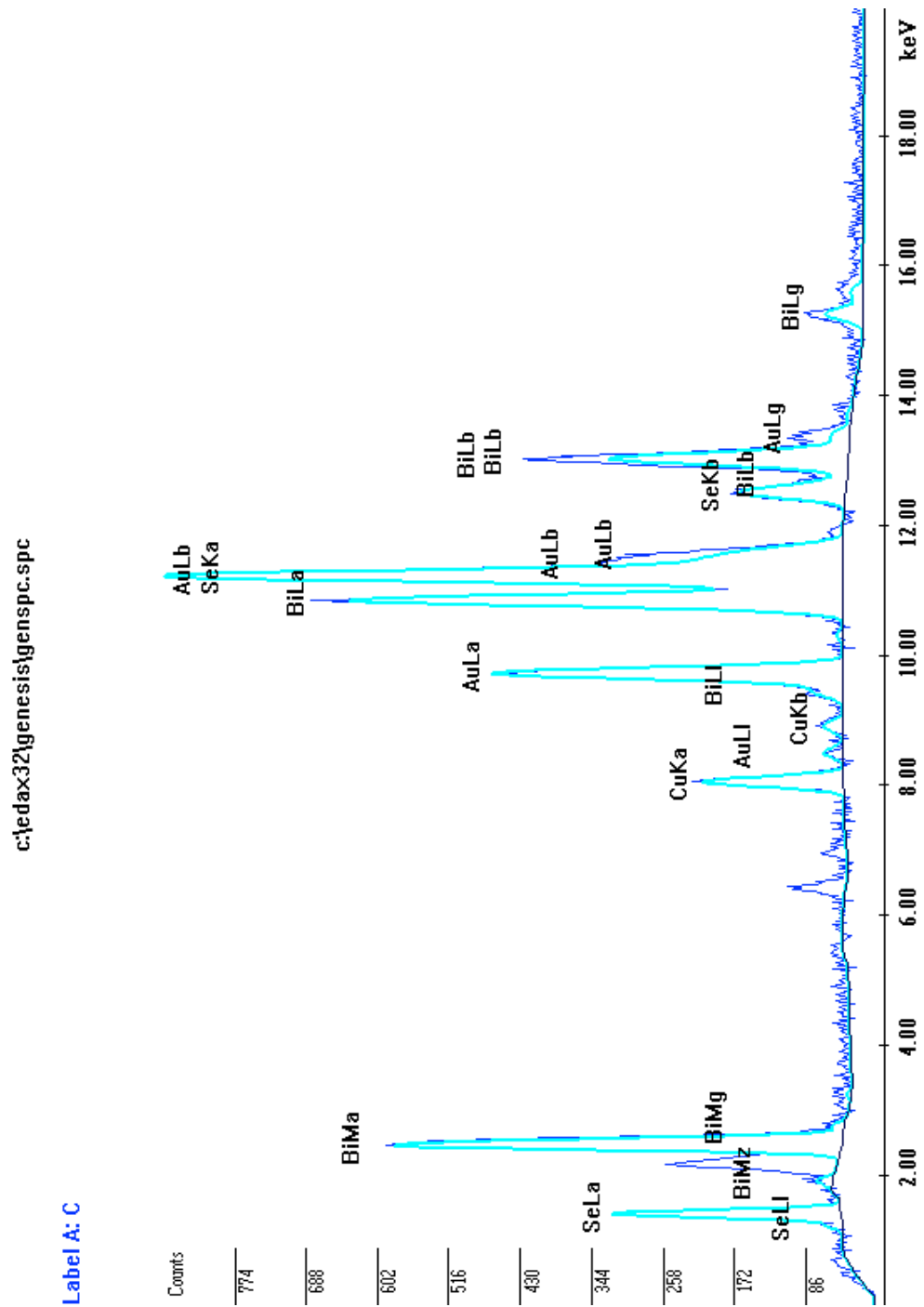HRTEM images of two different such regions on two different samples are shown in fig (2.3.1.ii). One of them is obtained out of microtome sections of 50nm and the other 25 nm as mentioned in the figure. Note the image displaying interference patterns showing the quintuple layer sequence. These are cross-sectional samples of Bi_2Se_3.

For the Cu- Bi_2Se_3 samples, before we jump into EELS analysis of the core-loss regions, it is very important to identify first whether or not we can detect copper. And it is easily done using preliminary check with the EDS. Fig (2.3.1.iii) is a typical example of EDS data indicating the presence of Cu. The other peaks corresponding to the Au-grid, Bi and Se are also highlighted. Once this is done, we are ready to perform EELS experiments.

2.3.2   Core Loss EELS

In the interest of answering our second objective, we started with obtaining EELS spectra from Cu-Bi_2Se_3. We noticed a specific nature of the NEFS. There are quite a few articles in literature [24,25] that insist on a Cu^{+1} valence state for the interstitial doping and we decided to verify this claim too. Moreover core-loss information could also help us understand why on doping Cu (and to specific sites), the system turns topologically superconducting [26]. An important point to note here is that our initial attempts were at comparing the Cu-L_3 edge of Cu-Bi_2Se_3 with that of the respective oxides Cu(I)O and Cu(II)O. The match was very poor and we immediately realized this was a bad comparison because although the valence states may be similar, the Cu-O system and Cu-Se system were very different. Thus, we ordered reference samples of Cu(I)Se and Cu(II)Se. Fig (2.3.2.i) shows typical experimental Cu-L_3 edge obtained from EELS in diffraction mode. This is obtained for Cu-Bi_2Se_3, Cu(I)Se and Cu(II)Se.

22
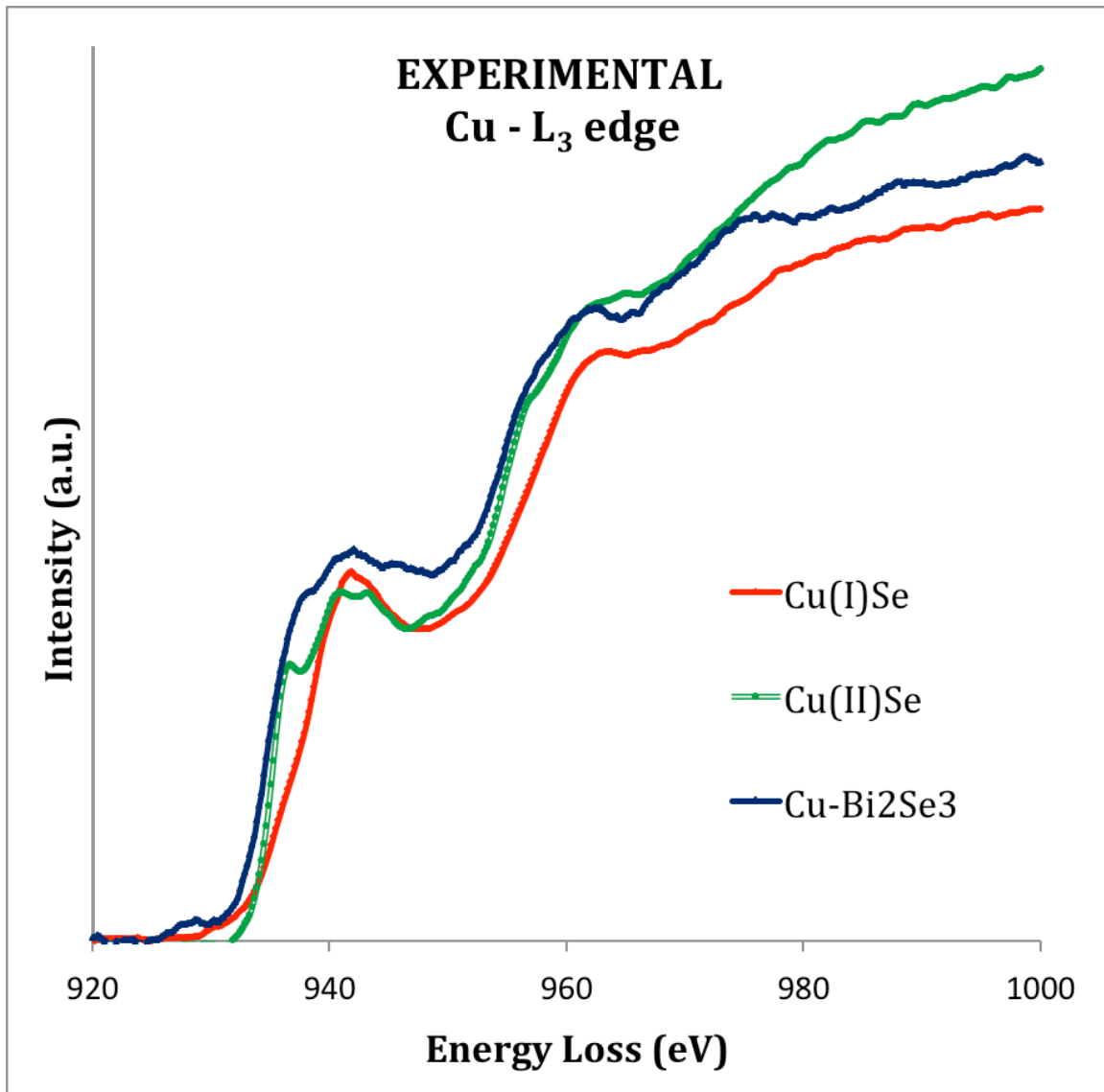
Fig (2.3.2.i) Experimental Cu-L$_3$ edge for Cu-Bi$_2$Se$_3$, Cu(I)Se and Cu(II)Se. From direct comparison of the three spectra it is not very easy to determine whether the blue spectra matches with red and green more. This may also suggest that Cu in Bi$_2$Se$_3$ might be a mixed valence state in between +1 and +2.

Right at this point we realized that TEM-EELS will not suffice to elaborate on the valence of Cu or its location in the atomic lattice. Instead, it led to more questions: (i) Is the valence closer to +1 or +2 or a mixed state of both? (ii) Is it first theoretically practical to embark on this experiment?

To answer these questions, we delved deeper into the core-loss analysis.

23

CHAPTER 3

CORE-LOSS ANALYSIS

3.1   Simulations

The moment we saw that after our first set of experiments we had more questions surrounding us, than answers, we decided that we must try to computationally attack this issue and understand what is at stake. So the first issue at hand was to simulate the NEFS for Cu for all the various systems we have and understand them.

3.1.1   FEFF8.4

The FEFF8.4 code [27,28] is a package that calculates the X-ray Absorption near-edge structure. The input for this code is generated by ATOMS program. What ATOMS does is generate atomic co-ordinates when crystallographic data about the crystal in question is fed as input. Now, the FEFF generated XANES spectrum is equivalent of EELS for x-rays and the LDOS that it calculates is the density of unoccupied states in the crystal. The FEFF code works on the RSMS technique in which it considers the atom of our choice as the central atom from which a spherical wave emanates. This wave, in its path outward, interacts with all its neighbors and thus reflects the 3 most important parameters that we are interested in, from an EEL spectrum:

a) Nature of neighbor (what element) - through the respective atomic potential

b) Nature of co-ordination (tetrahedral/octahedral) – spatial arrangement of atoms

c) Neighbor distance (bond length) – how strong/weak the interaction is.

3.1.1.1 ELNES

As mentioned earlier, the XANES output of the FEFF code is equivalent to the ELNES. So we start with the aim of simulating the Cu-L$_3$ ELNES for Cu(I)Se and Cu(II)Se so that we can use these to at least predict using simulations of the qualitative (and if possible quantitative) differences in the respective spectra amongst each other and with Cu-Bi$_2$Se$_3$. Interestingly, we observe that for every non-equivalent crystallographic position of an element, there is an associated NEFS that is unique to that position (as would be expected since the above mentioned three parameters would be different). Thus the overall NEFS of the system would be the weighted sum of all these states.

For ex: In Cu(II)Se there are two non-equivalent Cu sites (labeled **Type A** and **Type B**) in the unit cell, thus displaying two different NEFS [as in fig (3.1.1.1.i)]. And the cumulative spectrum (as it would be) is shown as **W.A x 1.75** (multiplied by a factor to plot it in a manner easy for comparison). The same is also done for Cu(I)Se. In this system, there are 'twelve' different sites of Copper. But they have been clubbed into four different types (Type: **A**, **B**, **C** and **D**) putting together sites with similar nearest neighbor co-ordination under one type. And looking at fig (3.1.1.1.ii) one can observe a similar variation in the NEFS of Cu for each of the types and also the overall spectrum as a weighted average. Here the overall spectrum has been shown as **W.A x 1.4.**

The above observation makes for an interesting argument since, it has been commonly presumed (as mentioned earlier) in many articles [24,25] that the 'Cu^{+1}' state contributes to doping in the intercalating regions in the Van der Waals gap. And this is also the specific site that contributes to the superconductivity at low temperatures in this otherwise non-superconducting system (at 5-10K).
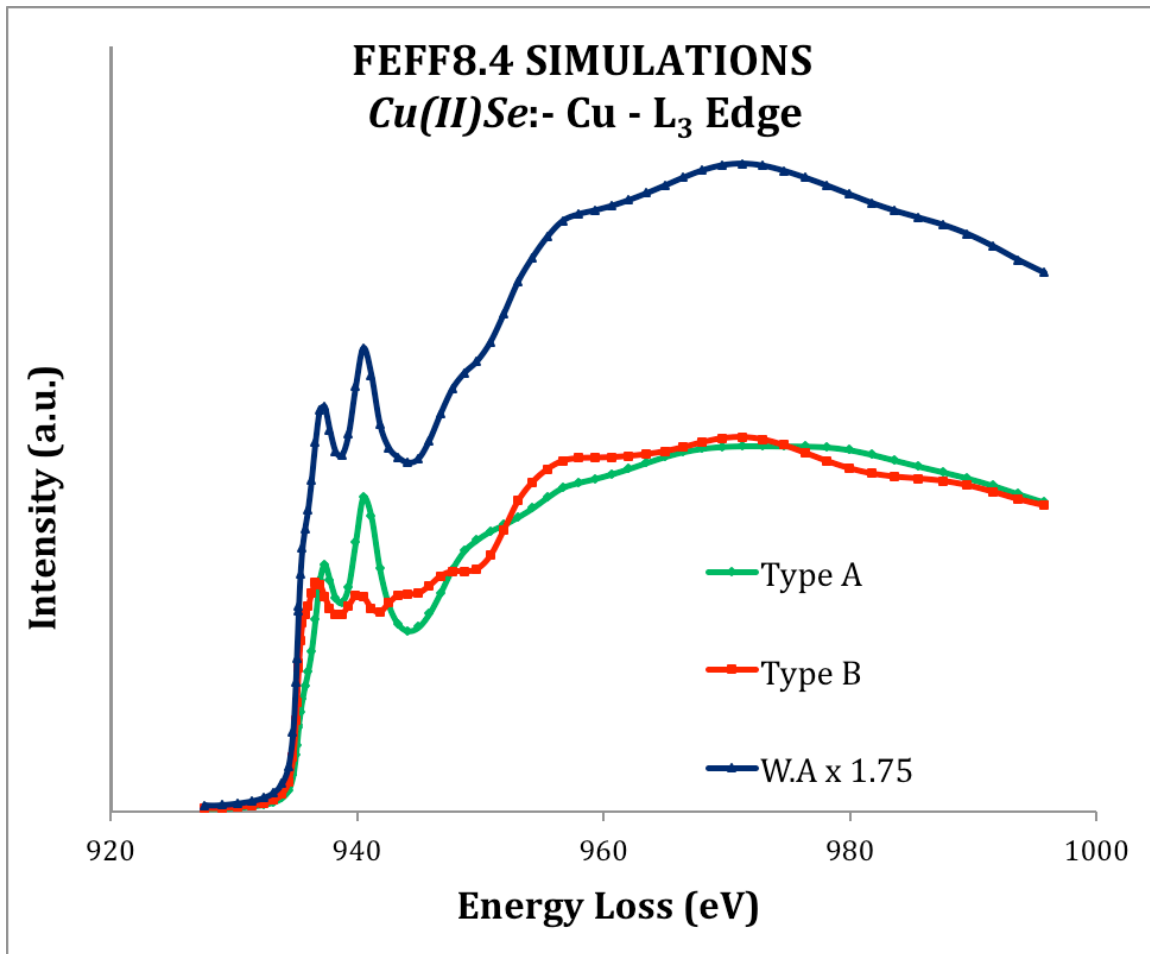
Fig (3.1.1.1.i) FEFF8.4 simulations of Cu-L$_3$ edge for Cu(II)Se. Type A and Type B refer to the two non-equivalent Cu atoms as the central atom for the calculation respectively. W.A refers to the weighted average of the aforementioned mentioned spectra which represents the overall spectrum. It is multiplied by a factor of 1.75 only for display. Notice the intensities of the two major peaks are completely reversed for the two cases!

EELS based valence determination for 3d elements [29,30] is a commonly found procedure, though in this case clearly, the NEFS cannot be attributed to a particular valence since it is not a one-one relation. Moreover, it also calls for a possible nearest neighbor co-ordination based classification of the dopant site, which would be more reliable and specific.
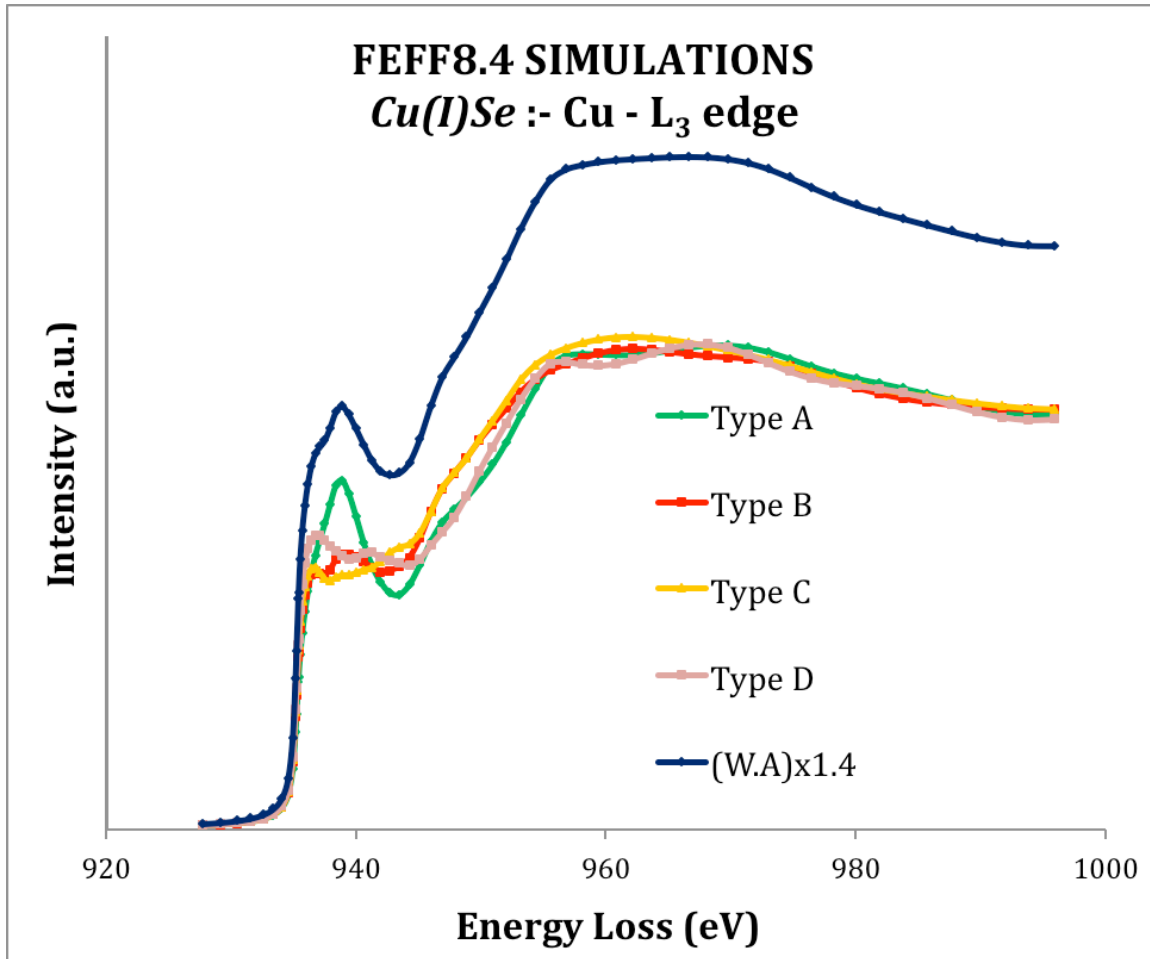
Fig (3.1.1.1.ii) FEFF8.4 simulations of Cu-L$_3$ edge for Cu(I)Se. Type A through D refer to the 12 different Cu atoms grouped together into four categories, that are each framed as the central atom for the calculation respectively. Like in Fig (3.1.1.1.i) W.A refers to the weighted average of the aforementioned mentioned spectra which would represent the bulk spectrum of Cu(I)Se. it is multiplied by a factor of 1.4 only for display.

3.1.1.2 DOS

FEFF8.4 apart from providing the NEFS for the central atom also provides the local density of states (DOS) for each element and for each orbital (s/p/d). We know that the NEFS in EELS/XAS is a direct consequence of the LDOS of the system. Thus it makes a good venture to analyse the LDOS and TDOS for the various cases mentioned below since that will help us understand what are the interacting orbitals and what is the

27

nature of interaction. Since the system in concern is Cu as central atom surrounded by Se

and Bi atoms as the nearest neighbors, our subsequent interest was in simulating the L-

DOS and T-DOS for various cases of neighbor co-ordination.

Fig (3.1.1.2.i) Cu-L_3 edge simulations for tetrahedral Cu [Type B Cu in Cu(II)Se]. The 4 nearest neighbors of Selenium are tetrahedrally co-ordinated. One by one it is substituted by Bismuth to observe the change in the NEFS as mentioned in the color code.

We study a tetrahedrally coordinated Cu as central atom. We start from a system

of purely Se nearest neighbors, substitute one nearest neighbor Se atom by Bi, to

ultimately result in a purely Bi nearest neighbor situation. This way, there is an extensive

library of NEFS and associated DOS for almost all possible cases of the specific

coordination.

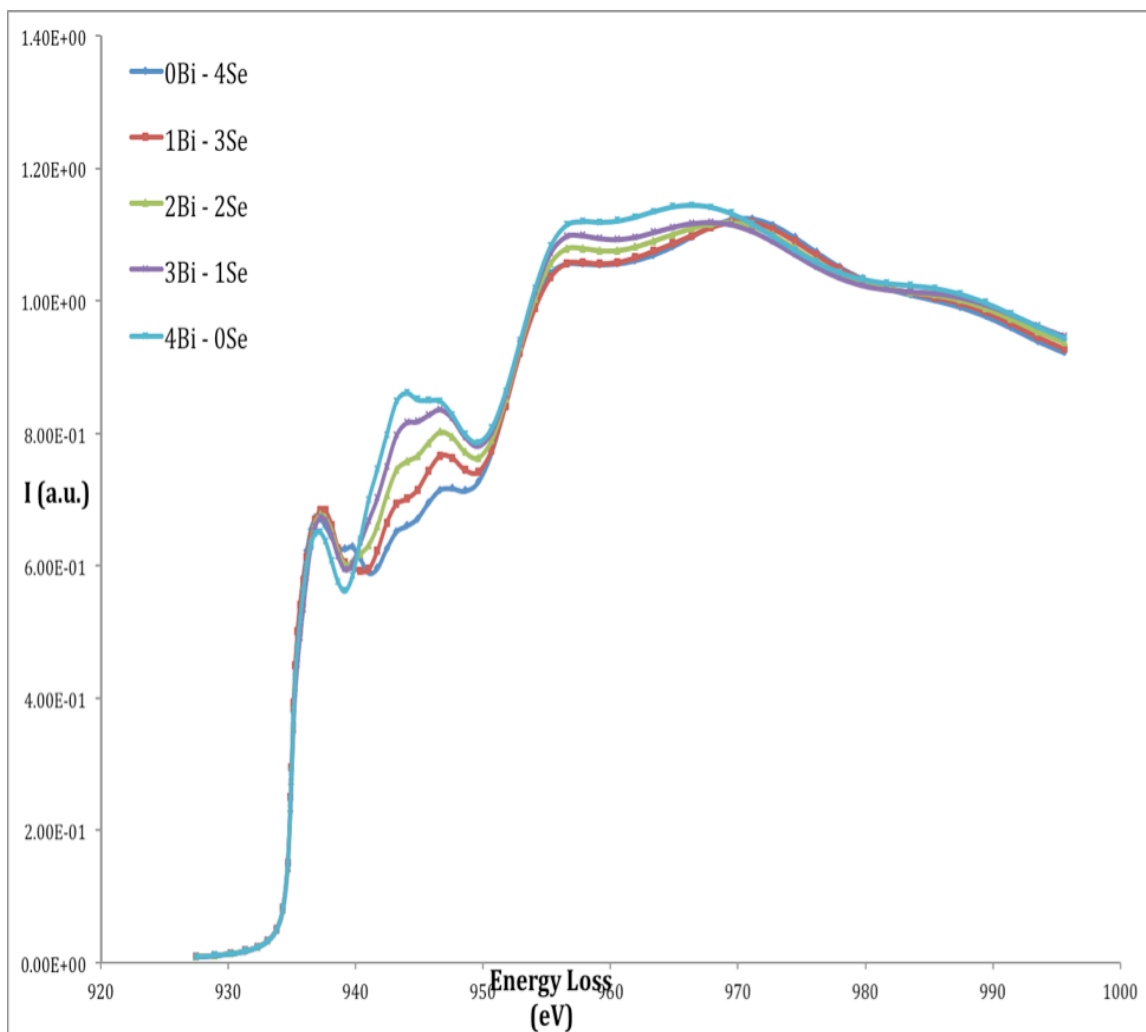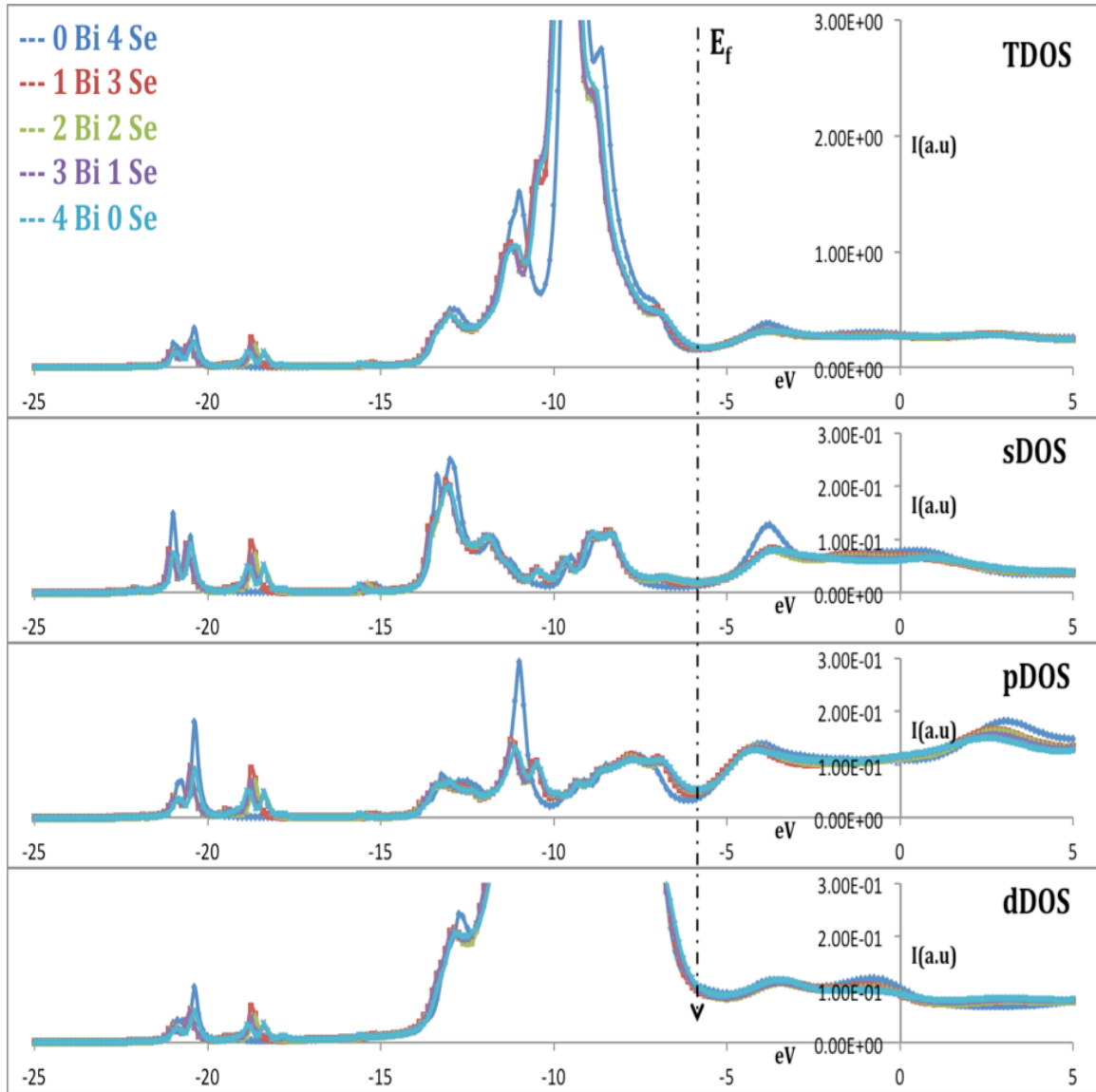Fig (3.1.1.2.ii) Partial (s, p, d) and total DOS simulations for tetrahedral Cu [Type B Cu in Cu(II)Se]. The 4 nearest neighbors of Selenium are tetrahedrally co-ordinated. One by one it is substituted by Bismuth to observe the change in the NEFS as mentioned in the color code. This figure goes in correlation with the NEFS simulations done in Fig (5). The dotted line marked in black denoted by E_f is the Fermi Energy. The Intensities are in arbitrary units and are adjusted so as to present the necessary features as best as possible. The Total DOS is the sum of the individual DOS for each particular case.

In fig (3.1.1.2.i) we present the ELNES simulations and in Fig (3.1.1.2.ii) the corresponding s-DOS, p-DOS, d-DOS and T-DOS for the case of tetrahedrally coordinated Cu(II)Se (with type B Cu as central atom). From the two figures, we can easily find the correlation of what we observe in the ELNES to what changes happen in the DOS. This will be held as a reference, which we will utilize when we can discover the nearest neighbor co-ordination in the actual system of interest Cu-Bi$_2$Se$_3$. Depending upon our observation from the experiments, if required, we might do a similar simulation series for the octahedral Cu system - substituting the Se atoms one by one with Bi.

The two issues that are very clear from simulations are − (a) that each non-equivalent site of Cu can possibly have a very different NEFS and so it will be wrong to advocate a valence comparison. Rather, for each different co-ordination, the NEFS will be unique and that would be a good standard. (b) Cu with majority Bi and Bu with majority Se neighbors have very different NEFS structures for the major two peaks after the edge. So obtaining a spectrum from Cu-Bi$_2$Se$_3$ and noticing the nature of the near-edge structure can be used to close in on the ideal co-ordination in the material of interest.

But before we push on to experiments, we have one more set of simulations to perform for comparison. And these must be the HAADF-STEM simulations for Cu(II)Se and Bi$_2$Se$_3$.

3.1.2 STEMSLICE

Simultaneous to the FEFF simulations, we also carried out STEM-HAADF image simulations using the STEMSLICE code to have an idea of what to expect in our actual experiments. Our motivation here is bi-directional:

- HAADF-STEM image simulation of Bi_2Se_3 – aligned with the primary goal of STEM-EELS experiments on Cu-Bi_2Se_3 [fig (3.1.2.i)].

- HAADF-STEM image simulation of Cu(II)Se – to distinguish the two non-equivalent Cu sites. Would be eventually useful if STEM-EELS from both these Cu sites were to be obtained experimentally [fig (3.1.2.ii)].
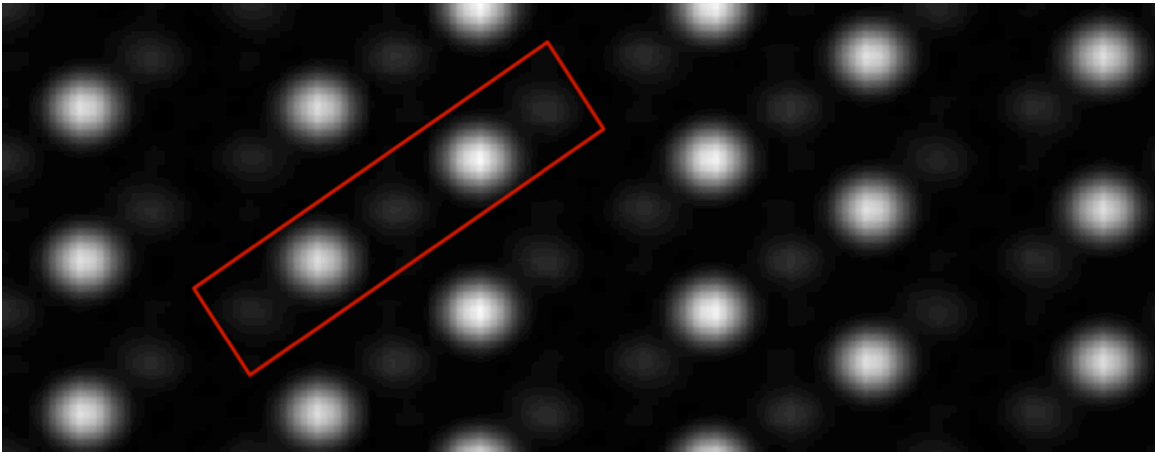

Fig (3.1.2.i) STEMSLICE simulation of HAADF-STEM images for cross-sectional Bi_2Se_3: Columns are well resolved. Brighter dots correspond to Bi and fainter dots correspond to Se. The red box denotes one quintuple layer of [Se-Bi-Se-Bi-Se]. Region between the two successive faint dots is the van der Waals region.
Simulation parameters: Projection = <100>; E_o = 200kV; C_s = 0.00mm; df = 0.00 A$^\theta$; Aperture = (0, 10.37) mrad; Size of ψ_{probe}: 256 x 256 pixels.

In the case of Bi_2Se_3 the atoms are clearly visible and thanks to the relatively large inter-atomic distances, the atoms are well separated. But as is visible in fig (3.1.2.i), ^{83}Bi being a huge atom scatters much stronger than ^{34}Se. In the eventuality of studying Cu-Bi_2Se_3, ^{29}Cu being the lightest element of the three, would probably be difficult to

identify purely through HAADF-STEM. The simulations thus present us a point of concern, a way to get over which would be HAADF-STEM + EDS/EELS.

Fig (3.1.2.ii) STEMSLICE simulation of HAADF-STEM images for cross-sectional Cu(II)Se: dumbbells observed. Relatively bigger atom in the dumbbell is Se. Inclined dumbbells contain Cu Type A and Vertical (horizontal) dumbbells contain Cu Type B. Note that Cu type A and Cu type B actually end up closer together in this orientation. Simulation parameters: Projection = <100>; E_o = 200kV; C_s = 0.00mm; df = 0.00 A^θ; Aperture = (0, 10.37) mrad; Size of ψ_{probe}: 256 x 256 pixels.

For the Cu(II)Se, the simulations show us that the Cu and Se atoms are too close to be separated perfectly. This means that we should be expecting a dumbbell like structure in our experiments too. But the two different Copper sites are a part of two different dumbbells and thus well differentiated. Thus if we can obtain EELS spectra from dumbbell set that are horizontal and those that are inclined separately, we must ideally be able to obtain two different Cu L_3 NEFS.

Here we would like to mention that we do not perform these simulations for Cu(I)Se. The reason to go only with Cu(II)Se was because, it seemed practically easier to work on Cu(II)Se considering it has only 'two' non-equivalent Cu sites within its unit cell as opposed to Cu(I)Se that has 'twelve'.

3.2   AC-STEM

With the simulation of the HAADF-STEM images and the NEFS and DOS with us, we first utilized the JeoL ARM200F instrument. It has a Cs corrector installed. This is TEM/STEM instrument and has significantly higher current in the STEM mode than the Nion UltraSTEM^{TM}100MC. Our aims getting into the experiments were:

- HAADF-STEM (EELS) on Cu(II)Se – To separate the two Cu sites and if possible obtain the individual EELS spectra from the respective sites.

- HAADF-STEM (EELS) on Cu-Bi$_2$Se$_3$ – Aligned with the primary aim to identify the site occupancy of Cu and also the nature of the Cu-NEFS (in this case atomic-column resolved).
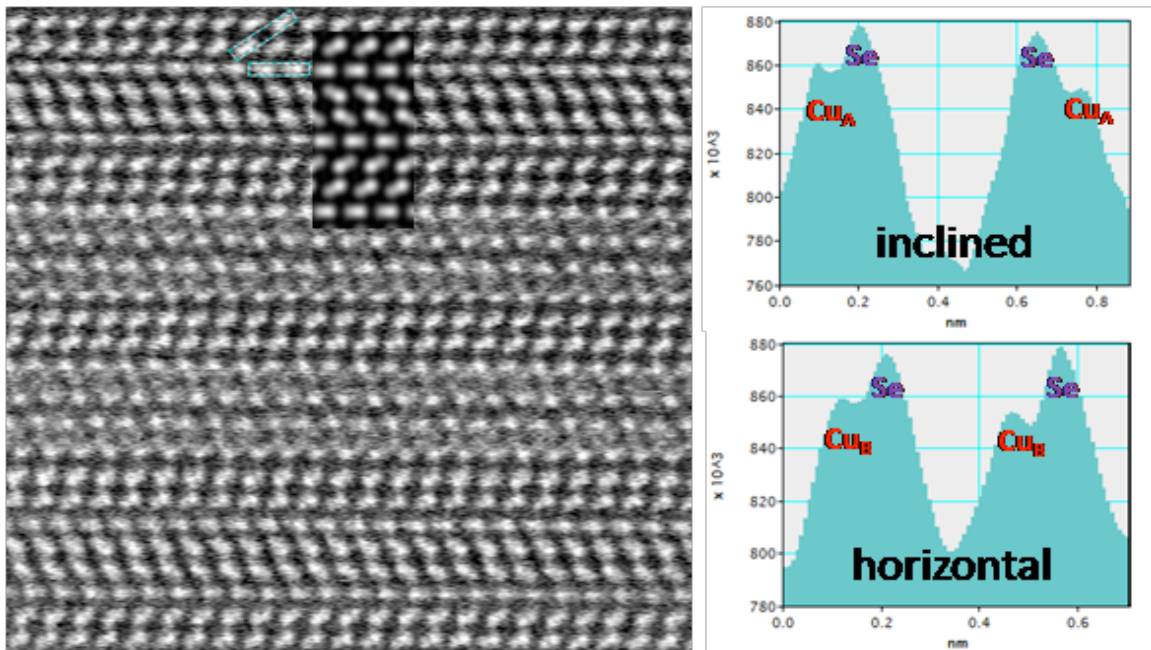

Figure (3.2.i) AC-STEM HAADF image of Cu(II)Se. LEFT: The image within the yellow box is the superimposed STEMSLICE simulation. It shows a very good match with experimental result. The two ROIs are the line plots integrated over a thickness of 20 units and their respective plots are on the RIGHT side of the HAADF image. The dumbbells are well resolved and going by the intensity variation, the smaller intensity corresponds to Cu and vice versa, as has been labeled in the line plots. The order of atom arrangement within the dumbbell is also visible thus.

Fig (3.2.i) shows a HAADF-STEM image of Cu(II)Se and a line profile from the image resolving the two dumbbells into their respective Se and Cu peaks. This can be compared with the STEMSLICE simulations performed (as in previous section) and are observed to match very well. We can also notice the stronger and weaker reflections in the dumbbells in the experiments as in our simulations. We would like to mention here that although in the line-plots that we show here, the intensity variation is clear and looks consistent, it is not the case for every region even within the displayed image fig (3.2.i). We think this is because, locally, not every region is perfectly aligned to the ZA. This is common in microtome prepared samples as compared to mechanically polished samples.

Having resolved the two Cu sites in Cu(II)Se, we were now interested in trying to obtain the NEFS data from the two different Cu sites that could potentially not just spatially resolve the Cu, but also attribute their individual and unique electronic structure identities. Albeit our efforts, for now, we have not been able to obtain any significant difference in the NEFS of the two different types of Cu. We strongly believe that this could be due to the much attributed 'cross-talk' between neighboring atomic columns that are not so far from each other (in this case around 2.2 A° apart). This has been explained in detail in the work by Dr. Rossouw [31,32] and Dr. Steve Pennycook's group [33]. Our case being further hindered since both the dumbbells in question contain Cu, the intensity of the Cu NEFS will not reduce/increase dramatically enough to observe a difference. Fig (3.2.ii.TOP) shows the two survey image with the two different EELS acquisition regions and fig (3.2.ii.BOTTOM) is both these spectra overlaid – no appreciable difference at all!
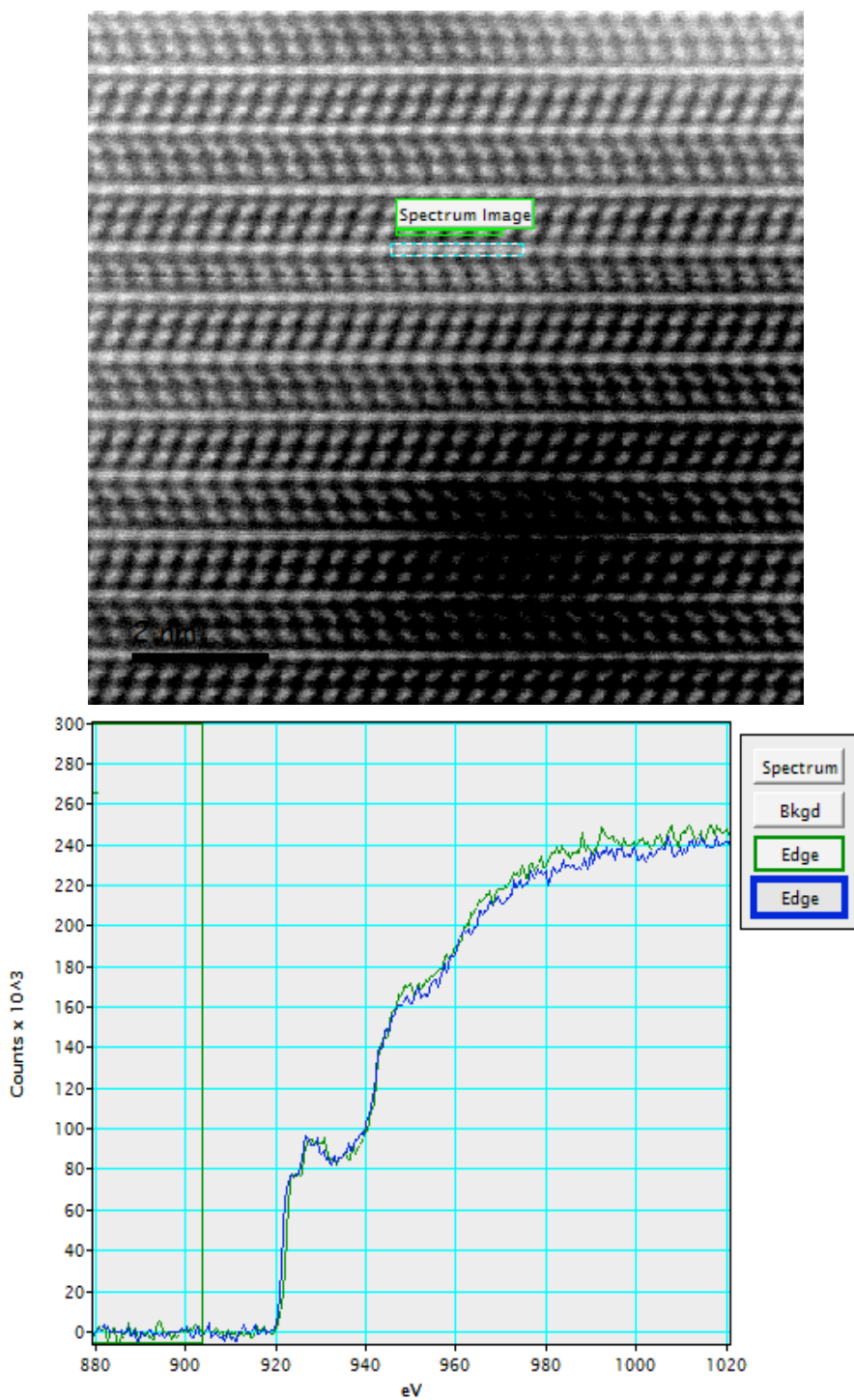
Figure (3.2.ii) STEM-EELS on Cu(II)Se. TOP: AC-STEM HAADF survey image of Cu(II)Se for EELS data acquisition. The green and the blue ROIs are respectively the inclined and the horizontal regions containing the two different types of Cu [as in fig (3.2.i)]. BOTTOM: The background subtracted EEL spectra of the respective cases. The two individual spectra (green and blue) are overlaid. Clearly there is no observable difference in intensity, peak width or nature/position of the peaks.

35

Fig (3.2.iii) shows Cu-L_3 edge from Cu-Bi$_2$Se$_3$. There were issues of mechanical stability on the ARM 200F and so even though the beam diameter was < 2A°, we do not know for sure about the region of scan. Moreover, as is evident from the spectrum, there is a lot of noise and so the fine-structure cannot be confidently interpreted. However, the fact that we observe a Cu-L_3 edge is a positive gain from the experiment. But we would like to mention here that since the probe was drifting, the localization of the beam was not good enough to claim a specific atomic-column location as the origin of the signal.
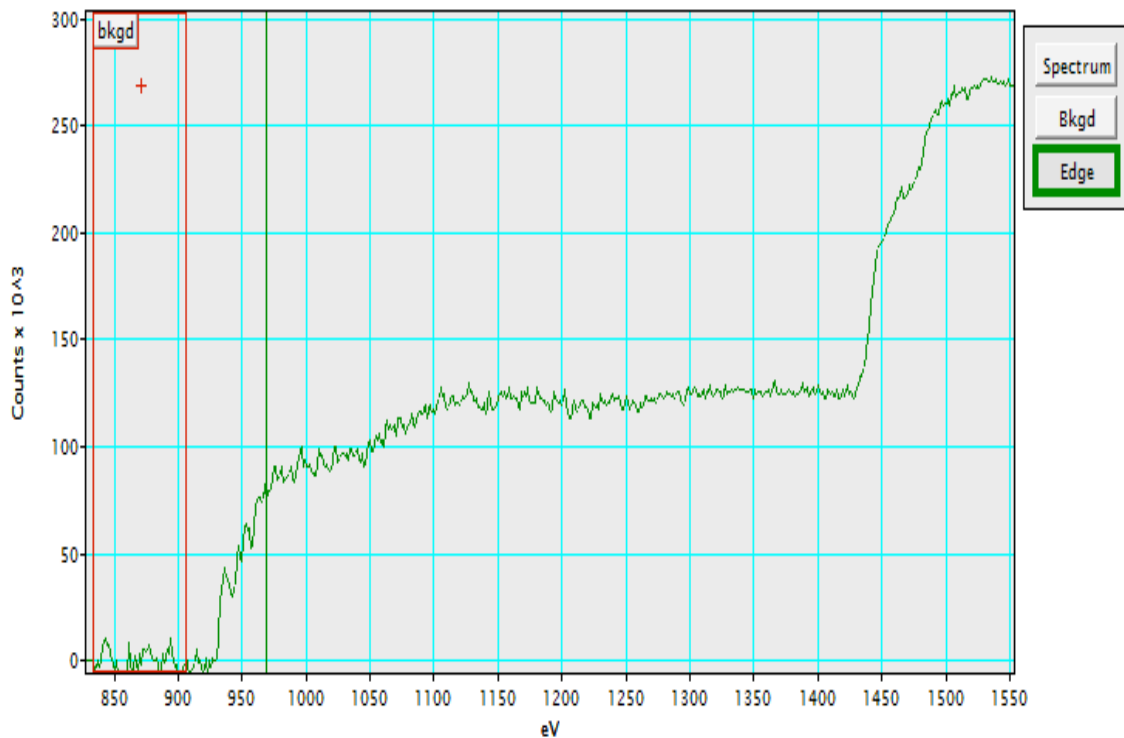
Figure (3.2.iii) STEM-EELS on Cu-Bi$_2$Se$_3$. Background subtracted edge shows presence of both Cu-L_3 edge and Se-L_3 edge. Since the noise is pretty high, it will be tough to interpret the fine-structure for Cu-L_3 from this spectrum. On the other hand, the exposure was already high to contaminate the sample within a few seconds of exposure. So higher acquisition time is not possible either. Shifting to Nion UltraSTEM may serve better.

CHAPTER 4

LOW LOSS ANALYSIS

4.1 AC-STEM

Apart from the interest in studying the core-level excitations in doped TIs, as has been mentioned right at the beginning, our interest is also in studying the vibrational and low-loss spectrum of Bi_2Se_3. As mentioned in the introduction, Bi_2Se_3 has a band gap of around 0.32eV and most of its optical phonon modes exist at <20 meV. Although the Nion UltraSTEM [2,34] has demonstrated capabilities of very high-energy resolution (30meV consistently), peaks around 50meV and lower (in absolute values of abscissa) would be nearly impossible to study because of the presence of the ZLP and its tail. But as can be seen in [20], there are lots of interesting electronic transitions happening in the low-loss regime. Moreover, this material has not been studied in such great detail using high resolution (S)TEM. So most of the electronic structure studies are from 70s and 80s. Bi_2Se_3 is known to have defects and although there is a moderate idea of the effect of the defects (anti-site Bi_{Se} and vacancies V_{Se}) [35], there is no study that specifically targets this issue to reports on the effect of the defects on the electronic states close to VB using a TEM. And apart from all these aspects, doping the Bi_2Se_3 sample can (and does) change the electronic structure around the valence band (since most of the electron transport happens from this region). Thus we pursued low-loss regime electronic-transition studies in Bi_2Se_3.

Fig (4.1.i) is a HAADF-STEM image of the sample with the STEMSLICE simulated image overlaid. The experimental atom centers are marked with red (Bi) and blue (Se) dots to visualize how good the agreement is qualitatively. Again, a point to note

is that since the samples are made by microtomy, very small and local changes in orientation is possible, thus shifting away from the ZA and hence not being perfectly aligned.
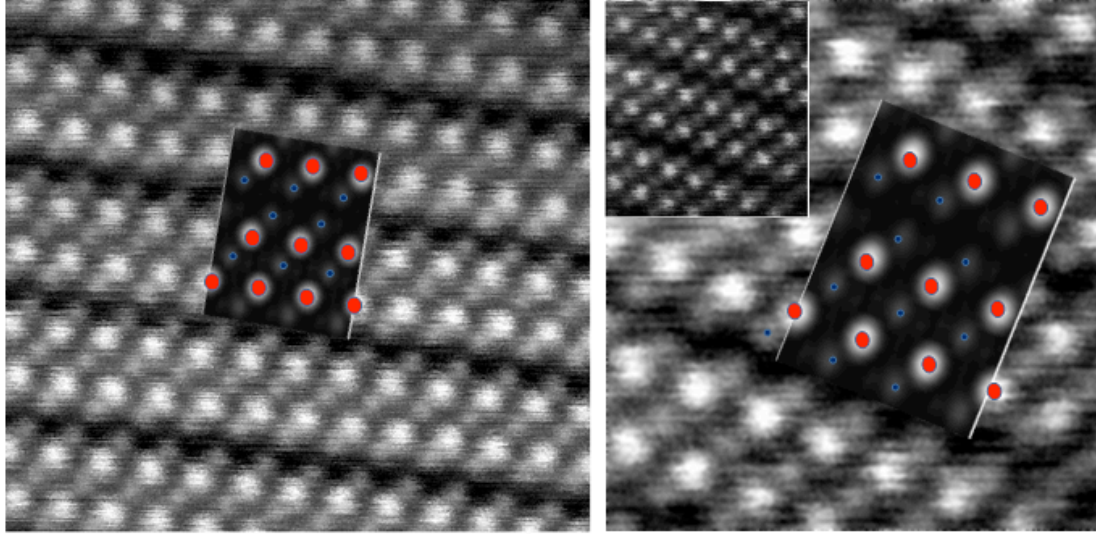

Fig (4.1.i) Experimental HAADF-STEM image of cross-sectional Bi_2Se_3. LEFT: Area 1 raw HAADF-STEM image and RIGHT: Area 2 smoothed-image with Inset on top left as the raw image. Overlaid image is STEMSLICE simulated image for both areas. Bright spots on the experimental image correspond to Bi, the other corresponds to Se.
Experiment Parameters: E = 100keV; MC not inserted; Convergence Semi-angle = 30mrad; Beam Current = 70-80 pA; Probe Size ≈ 1.2 A°
Simulation Parameters: E = 200 keV; Cs = 0mm; df = 0 A°; Aperture = 0, 10.4mrad; Size of probe ψ (Nx, Ny) = 512x512 pixels; Collection Detector = 50, 200 mrad; $(x_i, x_f, y_i, y_f, Nx_{out}, Ny_{out})$ = (0, 28, 0, 10.6, 64, 64).

Similar to [20] we also performed low-loss measurements at 0.02ev/channel and 0.1ev/channel. It was necessary to use a lower dispersion to obtain a bigger range on the energy loss. Choosing a higher dispersion gave higher resolution but the energy loss range was smaller due to the fixed number of pixels on the detector. As we can see in fig (4.1.ii.a and 4.1.ii.b), we are able to identify various kinds of electronic transitions like
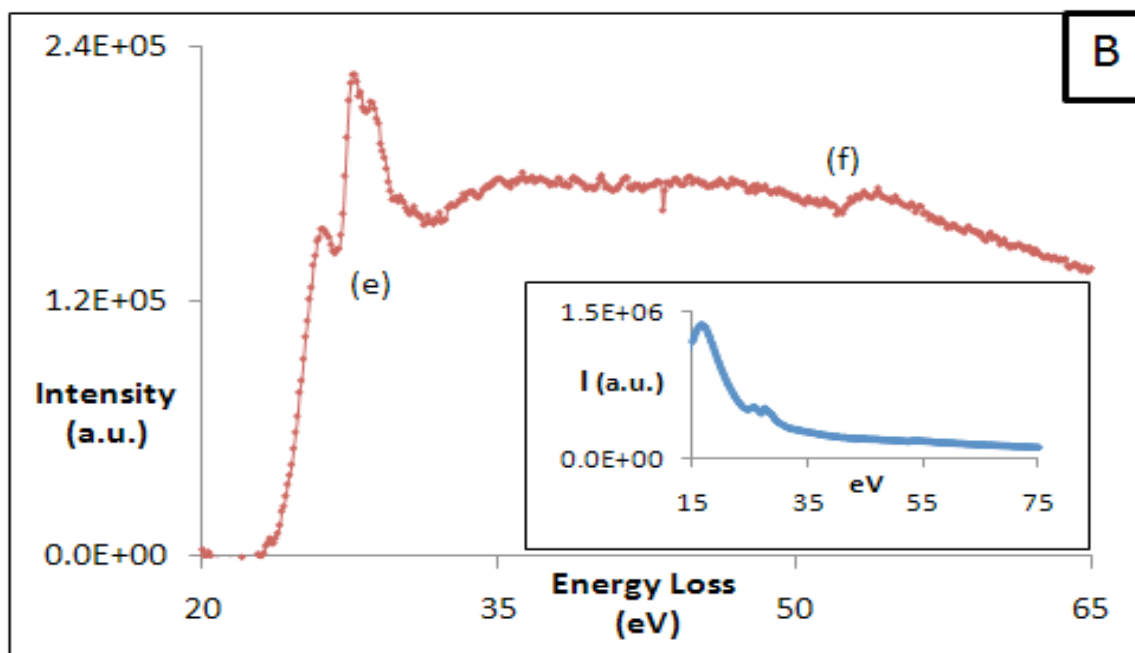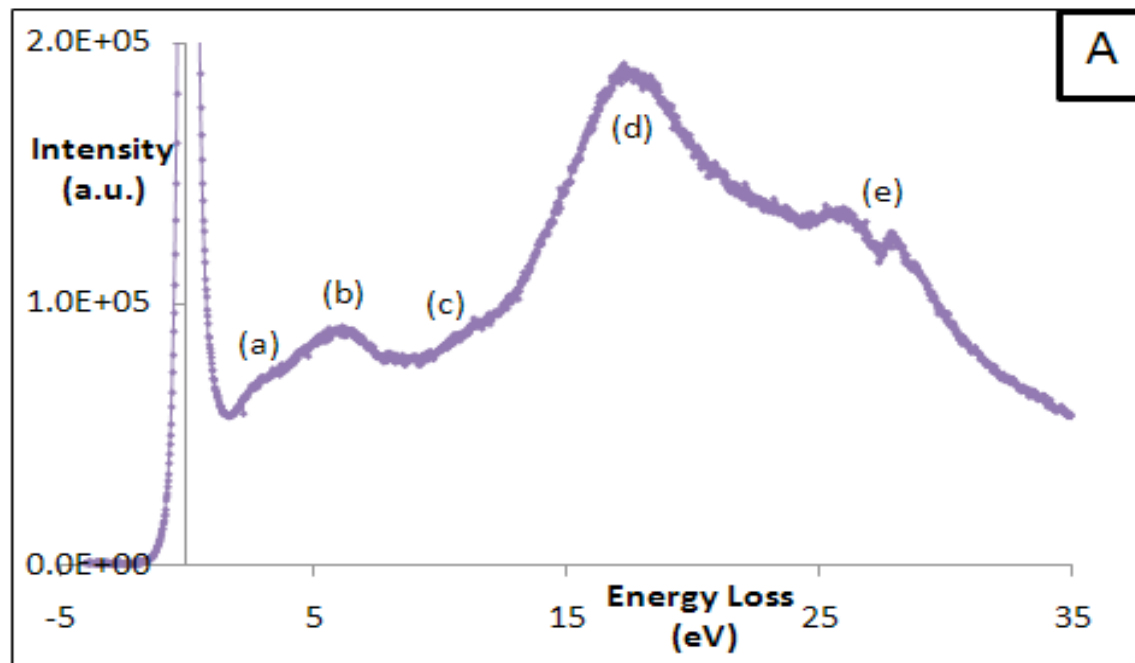
Fig (4.1.ii) Experimental low-loss STEM-EELS of Bi_2Se_3. A: Raw spectrum showing 5 peaks:- (e) is the Bi-$O_{4,5}$ peak. (d) and (b) are $\pi+\sigma$ and the π bulk plasmons respectively. (c) is predicted to be a surface plasmon. (a) is unknown at 2.5-2.8eV. B: Background subtracted spectrum with peaks (e) as above, and (f) as the Se-$M_{4,5}$ peak. Inset in the bottom-right shows the raw image.

Experiment Parameters: E = 100keV; MC inserted!; Convergence Semi-angle = 30mrad; EELS Collection angle = 15 mrad; Energy Resolution = 30 – 50 meV (ZLP FWHM); Beam Current = 50-70 pAmp; Probe Size $\approx$ 1.5 A°

the bulk plasmons (b) and (d); surface plasmons (c); $O_{4,5}$ edge of Bismuth (e) and $M_{4,5}$ edge of Selenium (f). There is also a peak (a) at around 2.5-2.8eV whose origin is unknown to us for now. The Bi-$O_{4,5}$ edge is actually very well observed in this spectrum.

Operating at the best energy resolution possible of around 40meV and 0.003eV/channel, we tried to observe the phonon region of the low-loss i.e. < 2eV (and specifically <0.5eV). We found an interesting feature as a shoulder on the tail of ZLP. We repeated the experiments and found it to be around the same value of roughly 0.32eV! We predict this to be the band-gap in which case it will be the first ever successful demonstration of identifying a band-gap at such low eV using a TEM.

We would like to highlight the figure (4.1.iii) all together to mention a few things. In spectrum (4.1.iii.a) the peak labeled (g) corresponds to the band-gap and the same peak post background subtraction of the ZLP is as observed in fig (4.1.iii.c). Figure (4.1.iii.b) is the ZLP recorded just before the measurement was made and it shows a FWHM (Δ) of 0.045eV (45 meV). In spite of that, we can still see a bulge on the lower end of the ZLP and this is probably due to aberrations that could not be corrected for during ELS spectrometer alignment.
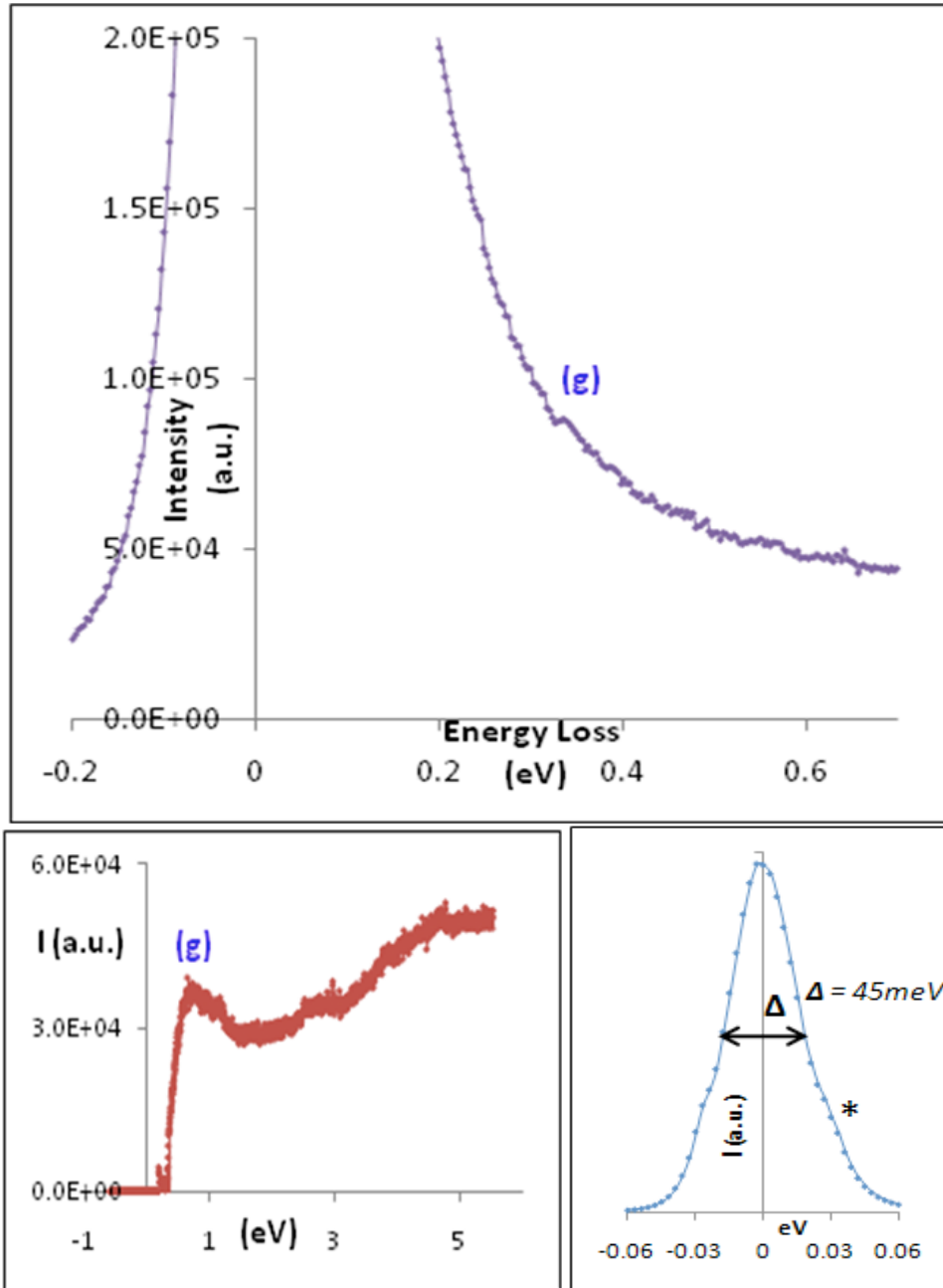
Fig (4.1.iii) Experimental Zero-Loss region STEM-EELS of Bi_2Se_3. TOP: Raw spectrum showing (g) band-gap transition peak. BOTTOM LEFT: background subtracted data of A clearly showing the transition at 0.32eV. BOTTOM RIGHT: ZLP measured just before the spectrum A was measured. Δ (FWHM) = 45meV and * is tail broadening due to ELS spectrometer aberration.

Experiment Parameters: E = 100keV; MC inserted!; Convergence Semi-angle = 30mrad; EELS Collection angle = 15 mrad; Energy Resolution = 30 – 50 meV (ZLP FWHM); Beam Current = 50-70 pAmp; Probe Size ≈ 1.5 A°

CHAPTER 5

CONCLUSIONS AND FUTURE ROADMAP

5.1   CONCLUSIONS

- Successful realization of TEM sample preparation process using ultramicrotome for Bi_2Se_3, Cu(I)Se and Cu(II)Se bulk crystals.

- Core-loss EELS in diffraction mode shows the dopant Cu does not match closely with Cu^{+1} or Cu^{+2} valence state.

- FEFF8.4 simulations reveal that every non-equivalent site possesses a unique NEFS. Thus, the overall FS for an atom in a crystal is a weighted average of such individual contributions. This means, classification based on co-ordination is a better and unique standard.

- Core-Loss (AC)STEM-EELS of Cu(II)Se shows cross-talk of the two copper sites.

- Low-Loss (AC)STEM-EELS using Nion reveals band-gap of Bi_2Se_3! And many other electronic transitions.

5.2   FUTURE ROADMAP

- Angle-resolved EELS in Nion-UltraSTEM to study unknown peak (a).

- Effect of doping on the low-loss inter/intra band transitions

- Study alternative (heavy) dopants to obtain HAADF-STEM images of dopant atomic positions.

- Correlate core-loss simulations using FEFF and STEM-EELS from $Cu-Bi_2Se_3$ to predict co-ordination around dopant atom.

REFERENCES

1.   Egerton, R. F. *Electron Energy-Loss Spectroscopy in the Electron Microscope*. (Plenum Press, New York, 1996).

2.   Krivanek, O. L., Lovejoy, T. C., Dellby, N. & Carpenter, R. W. Monochromated STEM with a 30 meV-wide, atom-sized electron probe. *Journal of electron microscopy* **62,** 3–21 (2013).

3.   Hsieh, D. *et al.* A topological Dirac insulator in a quantum spin Hall phase. *Nature* **452,** 970–4 (2008).

4.   Qi, X.-L. & Zhang, S.-C. Topological insulators and superconductors. *Reviews of Modern Physics* **83,** 55 (2010).

5.   Klitzing, K. v., Dorda, G. & Pepper, M. New method for high accuracy determination of fine-struture constant based on quantized hall resistance. *Physical Review Letters* **45,** 11–14 (1980).

6.   Kane, C. L. & Mele, E. J. Z_{2} Topological Order and the Quantum Spin Hall Effect. *Physical Review Letters* **95,** 146802 (2005).

7.   Kane, C. L. & Mele, E. J. Quantum Spin Hall Effect in Graphene. *Physical Review Letters* **95,** 226801 (2005).

8.   Bernevig, B. A., Hughes, T. L. & Zhang, S.-C. Quantum spin Hall effect and topological phase transition in HgTe quantum wells. *Science (New York, N.Y.)* **314,** 1757–61 (2006).

9.   König, M. *et al.* Quantum spin hall insulator state in HgTe quantum wells. *Science* **318,** 766–70 (2007).

10.   Fu, L., Kane, C. & Mele, E. Topological Insulators in Three Dimensions. *Physical Review Letters* **98,** 106803 (2007).

11.   Qi, X. & Zhang, S. The quantum spin Hall effect and topological insulators. *Arxiv 1001.1602v1* (2010).

12.   Zhang, H. *et al.* Topological insulators in Bi2Se3, Bi2Te3 and Sb2Te3 with a single Dirac cone on the surface. *Nature Physics* **5,** 438–442 (2009).

13.   Horak, J., Stary, Z., Lostak, P. & Pancir, J. ANTI-SITE DEFECTS IN n-Bi,Se, CRYSTALS. *J. Phys. Chem. Solids* **51,** 1353–1360 (1990).

14.   Hor, Y. S., Checkelsky, J. G., Qu, D., Ong, N. P. & Cava, R. J. Superconductivity and non-metallicity induced by doping the topological insulators Bi2Se3 and Bi2Te3. *J Phys Chem Solids* **72,** 572 (2011).

15.   Salman, Z. *et al.* The Nature of Magnetic Ordering in Magnetically Doped Topological Insulator Bi_2-xFe_xSe_3. *Arxiv Preprint* 1203.4850 (2012). at <http://arxiv.org/abs/1203.4850>

16.   Zhang, D., Richardella, A., Xu, S. & Rench, D. W. Interplay between ferromagnetism, surface states, and quantum corrections in a magnetically doped topological insulator. *Cond Mat* **arxiv:1206,** 1–18 (2012).

17.   Hor, Y. S. *et al.* Superconductivity in Cu_{x}Bi_{2}Se_{3} and its Implications for Pairing in the Undoped Topological Insulator. *Physical Review Letters* **104,** 057001 (2010).

18.   Wray, L. A. *et al.* Observation of topological order in a superconducting doped topological insulator. *Nature Physics* **6,** 855–859 (2010).

19.   Huang, F.-T. *et al.* Nonstoichiometric doping and Bi antisite defect in single crystal Bi_{2}Se_{3}. *Physical Review B* **86,** 081104 (2012).

20.   Liou, S. C. *et al.* Plasmons dispersion and nonvertical interband transitions in single crystal Bi_{2}Se_{3} investigated by electron energy-loss spectroscopy. *Physical Review B* **87,** 085126 (2013).

21.   Shu, G. J., Liou, S. C. & Chou, F. C. π -bonds in graphene and surface of topological insulator Bi2Se3. *Arxiv* 1–5 (2013).

22.   Das, T., Bhattacharyya, S., Prakash Joshi, B., Thamizhavel, A. & Ramakrishnan, S. Direct evidence of intercalation in a topological insulator turned superconductor. *Materials Letters* **93,** 370–373 (2013).

23.   Tafto, J. & Zhu, J. Electron Energy Loss Near Edge Structure (ELNES), A potential technique in the studies of local atomic arrangements. **9,** 349–354 (1982).

24.   Kriener, M. *et al.* Electrochemical synthesis and superconducting phase diagram of Cu_{x}Bi_{2}Se_{3}. *Physical Review B* **84,** 054513 (2011).

25.   Vasko, A., Tichy, L., Horak, J. & Weissenstein, J. Amphoteric nature of copper impurities in Bi2Se3 crystals. *Appl. Phys* **5,** 217–221 (1974).

26.   Bray-Ali, N. & Haas, S. How to turn a topological insulator into a superconductor. *Physics* **3,** 11 (2010).

27. Ankudinov, A. L., Ravel, B., Rehr, J. J. & Conradson, S. D. Real-space multiple-scattering calculation and interpretation of x-ray-absorption near-edge structure. **58,** 7565–7576 (1998).

28. Moreno, M. S., Jorissen, K. & Rehr, J. J. Practical aspects of electron energy-loss spectroscopy (EELS) calculations using FEFF8. *Micron (Oxford, England : 1993)* **38,** 1–11 (2007).

29. Paterson, J. H. & Krivanek, O. L. ELNES OF 3d TRANSITION-METAL OXIDES H. Variations with oxidation state and crystal sffucture James H. PATERSON. *Ultramicroscopy* **32,** 319–325 (1990).

30. Wang, Z., Yin, J. & Jiang, Y. EELS analysis of cation valence states and oxygen vacancies in magnetic oxides. *Micron (Oxford, England : 1993)* **31,** 571–80 (2000).

31. Findlay, S. D., Allen, L. J., Oxley, M. P. & Rossouw, C. J. Lattice-resolution contrast from a focused coherent electron probe. Part II. *Ultramicroscopy* **96,** 65–81 (2003).

32. Rossouw, C. J., Allen, L. J., Findlay, S. D. & Oxley, M. P. Channelling effects in atomic resolution STEM. *Ultramicroscopy* **96,** 299–312 (2003).

33. Allen, L., Findlay, S., Lupini, A., Oxley, M. & Pennycook, S. Atomic-Resolution Electron Energy Loss Spectroscopy Imaging in Aberration Corrected Scanning Transmission Electron Microscopy. *Physical Review Letters* **91,** 105503 (2003).

34. Krivanek, O. L. *et al.* High-energy-resolution monochromator for aberration-corrected scanning transmission electron microscopy/electron energy-loss spectroscopy. *Philosophical transactions. Series A, Mathematical, physical, and engineering sciences* **367,** 3683–97 (2009).

35. Taylor, R. E., Leung, B., Lake, M. P. & Bouchard, L.-S. Spin–Lattice Relaxation in Bismuth Chalcogenides. *The Journal of Physical Chemistry C* **116,** 17300–17305 (2012).